International Journal of Non-Linear Mechanics 101 (2018) 95–112

Contents lists available at ScienceDirect

International Journal of Non-Linear Mechanics

journal homepage: www.elsevier.com/locate/nlm

An objective multi-scale model with hybrid injection

Nicolás A. Labanda [a,b,*], Sebastián M. Giusti [d,e], Bibiana M. Luccioni [c,e]

[a] Universidad de Buenos Aires, Facultad de Ingeniería, Grupo LMNI, Buenos Aires, Argentina
[b] SRK consulting, Buenos Aires, Argentina
[c] Structure Institute, National University of Tucumán, Av. Independencia 1800, San Miguel de Tucumán CP 4000, Argentina
[d] GIDMA, Department of Civil Engineering, National Technological University, Maestro M. López esq. Cruz Roja, Córdoba X5016ZAA, Argentina
[e] CONICET, Av. Rivadavia 1917, Buenos Aires, Argentina

ARTICLE INFO

Keywords:
Multi-scale model
Numerical homogenization
Representative volume element
Cohesive model
Composites materials

ABSTRACT

This paper presents a new semi-concurrent multi-scale model to study the behaviour of composite materials in softening regime. A mixed formulation is used to simulate discontinuities in both scales. The traction over the crack is included as a unknown field in the equations system of the problem, and the jump displacement across the discontinuity is obtained with a cohesive constitutive relation (traction-separation law).

Axiomatic variational principles and the injection concept are used and formulated to get an objective model with respect to the representative volume element size (**RVE**). The projected stress over the normal vector of the macro discontinuity is injected in the localized domain in the **RVE**, obtaining as a dual variable the jump of the displacement field in the macro structure. In this way, during the stable phase of the behaviour, the scale transition is performed in the classical way injecting the strain tensor and obtaining the stress tensor as a dual variable. At the beginning of the unstable regime, the transition between the scales is defined by injecting the traction (stress projection on the normal vector to the crack) in the localization domain in the micro scale and the displacement jump at the macro scale is obtained as a dual variable. This new concept leads to a new multi-scale approach with an hybrid injection.

The basic equations of the model are derived, and finally some numerical examples are developed, showing the objectivity of the homogenized response of composite material problems that involve strain localization at the macro-scale.

1. Introduction

Multi-scale modelling is a trend research area in the computational mechanics community. This kind of models can be divided in two main groups: Multi-scale models based on *analytic methods* and those based on *computational methods*. Analytic methods can be classified in *continualization* methods and *homogenization* methods. In continualization methods, the micro/meso scale is considered as discrete elements like masses, springs or tribology elements, and Taylor series are used to define the transition to the macro-scale [1,2]. In *homogenization* methods the sub-scale is continuous and heterogeneous, while the macro-scale is continuous and homogeneous and they are normally used to obtain elastic properties at the macro-scale [3–8]. Analytic methods are nowadays being displaced by *computational multi-scale methods* that have greater versatility [9].

Park and Liu [10] and Oden at al. [11] proposed a classification of computational multi-scale modelling *hierarchical* and *concurrent* multi-scale models. Hierarchical approaches are normally used to calibrate constitutive equations while concurrent multi-scale models consider the different constituents of the composite at a lower scale.

Bohm [12] classified methods that couple continuum models in: *mean-field approximation methods* [13–15], *variational bounding methods* [16–18] and *methods based in the representative volume element (**RVE**) concept*. Methods based in the **RVE** concept can be divided in:

- Hierarchical methods: The material is constitutively described in some length scale by using an homogenization of a lower scale. These methods are adequate for materials that require a sequence of scales for their description, like laminated or bio-materials. Although this approach does not consider an unitary cell in its definition, it is used in most of the developed models [19–24]. Another approach that contains this type of hierarchical multi-scale models is that of *quasi-phenomenological* models in which an internal variable is calibrated using the **RVE** concept [25].

* Correspondence to: Universidad de Buenos Aires, Buenos Aires, Argentina.
E-mail address: nlabanda@facet.unt.edu.ar (N.A. Labanda).

https://doi.org/10.1016/j.ijnonlinmec.2018.01.009
Received 5 August 2017; Received in revised form 29 December 2017; Accepted 26 January 2018
Available online 7 March 2018
0020-7462/

- Semi-concurrent methods: These models insert a primary field (strain, temperature gradient, etc.) as a boundary condition in the **RVE**, relating both scales through a compatibility equation (generally an energy type equation). Once the boundary value problem in the micro-scale is solved, a constitutive tensor and an homogenization operator to obtain the dual variable (stress, thermal flux, etc.) is computed for the macro scale. These models are colloquially known as FE^2 models [26–31].
- Concurrent methods: In this kind of formulations the **RVE** is embedded in the zone of interest within the macro-scale. It has been used to couple continuum and atomic scales, where the fractured region is modelled by broken up inter-atomic forces [32,33]. When both scales are modelled by continuous formulations non-matching meshes can be used, getting the compatibility with Lagrange multipliers. This approach has the disadvantage of being computationally expensive when the length scale of the **RVE** is not close to the macro-scale length [34]. Some authors have used this approach to simulate concrete specimens [31,35].
- Hybrid methods: These methods involve a combination of concurrent and semi-concurrent approaches. Within a localization regime, semi-concurrent models generally become non-objective with respect to the **RVE** size. Hybrid models consider a semi-concurrent formulation for macro-scale zones in stable regime, while in unstable zones where a fracture is propagated or damage progress is spread, the **RVE** is embedded in the macro-structure. Akbari [36] proposed an hybrid multi-scale model for fracture analysis of polycrystallines materials.

During the last decades several sophisticated models based on the **RVE** concept, have been proposed for the simulation of quasi-brittle localization at the macro-scale. A formulation that calibrates damage evolution by using a **RVE** with classical interface elements and is able to model fracture evolution in mode I at the macro-scale, has been proposed by Verhoosel et al. [37]. This approach was latter expanded [38,39] for mixed fracture modes, considering cohesive and adhesive elements. Massart et al. [40] presented a continuous–discontinuous homogenization scheme using a first order computational homogenization (FOCH) with the capability of localizing the strain field in the macro-structure and they used it to study the failure mechanism of masonry. In the field of moderate localizations, a new kind of semi-concurrent multi-scale formulations was proposed by Kouznetsova et al. [41]. The strain gradient is transferred as a rotation on the boundary of the **RVE** arriving to a gradient enhanced method at the macro scale combined with a classical description for the micro-scale. This kind of formulations is known as second order homogenization scheme (SOCH) [42–44].

Some attempts to enhance FOCH models have also been published. A two-scale failure multi-scale model expressed as an expansion of the variational framework presented in [45], was presented by Toro et al. [46] introducing the *injection operator* concept proposed in [47]. The macro-scale jump, modelled using an E-FEM technology, is introduced as a boundary condition in the localized domain of the **RVE**. Analogously to the model proposed in [38], an homogenized traction-separation law is obtained. A similar approach has been developed for the analysis of quasi-brittle fracture processes using cohesive bands technology [48]. In this case, the localization band in the macro-scale is calibrated using a characteristic length obtained in the **RVE** and an objective regularization is achieved with this parameter.

This kind of FOCH enhanced models, represents a trend research area with many challenges. Debonding and matrix fracture phenomena in composites with strongly different stiffness can be analysed with mixed methods, like augmented Lagrangian formulations based on displacement and the crack tension, avoiding ill-conditioning problems associated with penalty methods [49,50]. Classic multiscale approach [45] or two-scale failure multi-scale model presented by Toro et al. [51] cannot be directly used in conjunction with mixed approaches to simulate discontinuities in the micro and macro-scale. A new semi-concurrent multi-scale model based on an hybrid injection, formulated in a consistent variational framework is proposed in this paper to simulate composite material failure. The novelty of this approach is that is obtained as a natural extension of the classic formulation [45] to the case of mixed approaches. The proposed multi-scale model involves a stress–strain description in the stable phase and a traction-separation law for the unstable regime. A classical multi-scale model is used to obtain the strain–stress relationship [45], while when an unstable phase is reached and the material starts a softening regime, a model that links localization in both scales injecting the traction at the macro-scale discontinuity in the RVE is presented. Lagrange multipliers representing tension at the fracture are treated like the kinematic field in the classic approach [45]. In this way the stress injection in the cracks corresponding to the localization domain of the RVE has a clear physical meaning and equations analogous to those obtained in one field approaches [45,46] are obtained. By the other side, it is well recognized that traction based boundary conditions can be more naturally introduced than periodic conditions in the localizing regime. In accordance to this observation, Coenen and co-workers [52,53] proposed the use of so called percolation-path-aligned boundary conditions that consist of a gradual transition from periodicity RVE boundary conditions towards more relaxed boundary conditions when localization is detected.

A mixed formulation based on the displacement and the crack tension, is used to simulate discontinuities in both scales and it is presented in Section 2. The proposed model, based on the axiomatic philosophy proposed in [26,47], is presented in Section 3. Some numerical examples, where the objectivity of the homogenized traction-separation law is shown, are presented in Section 4. Finally, conclusions and future trends in this research area, are drawn in Section 5.

2. Mixed formulation for quasi-brittle fracture simulation. A general background

A method based on a mixed functional that considers as unknown variables the displacement field and the crack traction field is used to simulate the fracture process in both scales. A brief description is presented in this section. More details can be found in [49,54].

2.1. Variational formulation

Let $\mathscr{L}^{\boldsymbol{u}} : \mathscr{U} \rightarrow \boldsymbol{R}$ be a system potential dependent on the displacement field $\boldsymbol{u}$ of a infinitesimally deformable body including a fracture Γ (see Fig. 1), expressed as:

$$\mathscr{L}^{\boldsymbol{u}}(\boldsymbol{u}) = \mathscr{L}^{\mathcal{B}}(\boldsymbol{u}) + \mathscr{L}^{\mathcal{F}}(\llbracket \boldsymbol{u} \rrbracket), \tag{1}$$

where $\llbracket \bullet \rrbracket = (\bullet)|_{\Gamma^+} - (\bullet)|_{\Gamma^-}$ represents the jump of the field $(\bullet)$ over the domain Γ. The potential of the bulk domain $\Omega = \Omega^- \cup \Omega^+$ is denoted with $\mathscr{L}^{\mathcal{B}}$ and $\mathscr{L}^{\mathcal{F}}$ is the fracture potential of the crack in Γ, that are defined as follows:

$$\begin{aligned} \mathscr{L}^{\mathcal{B}}(\boldsymbol{u}) &= \frac{1}{2}\int_{\Omega\setminus\Gamma} \boldsymbol{\sigma}(x,t) : \nabla^s \boldsymbol{u}(x,t)\ d\Omega - \int_{\Omega\setminus\Gamma} \boldsymbol{b}(x)\cdot\boldsymbol{u}(x,t)\ d\Omega \\ &\quad - \int_{\partial^t\Omega} \boldsymbol{p}(x,t)\cdot\boldsymbol{u}(x,t)\ d\partial^t\Omega \\ \mathscr{L}^{\mathcal{F}}(\llbracket \boldsymbol{u} \rrbracket) &= \int_{\Gamma} \Psi(\llbracket \boldsymbol{u} \rrbracket, \kappa)\ d\Gamma, \end{aligned} \tag{2}$$

being $\boldsymbol{b} \in \mathbf{L}^2(\Omega\setminus\Gamma)$ is the volumetric force, $\boldsymbol{\sigma}$ is the Cauchy stress tensor, $\nabla^s\boldsymbol{u}$ is the symmetric part of the displacement field gradient. In the Neumann boundary $\partial^t\Omega$ a distributed load $\boldsymbol{p} \in \mathbf{L}^2(\partial^t\Omega)$ is considered. In the Dirichlet boundary $\partial^u\Omega$ a prescribed displacement value $\bar{\boldsymbol{u}}$ is applied. The normal vector to the crack Γ is denoted as $\boldsymbol{n}$. The kinematically admissible set $\mathscr{U}(\Omega\setminus\Gamma)$ is defined as:

$$\mathscr{U}(\Omega\setminus\Gamma) = \{\boldsymbol{u} \in \mathbf{H}^1(\Omega\setminus\Gamma) \ \wedge\ \llbracket \boldsymbol{u} \rrbracket\cdot\boldsymbol{n} \geq 0 \in \mathbf{H}^{\frac{1}{2}}(\Omega) : \boldsymbol{u}|_{\partial^u\Omega} = \bar{\boldsymbol{u}}\}. \tag{3}$$

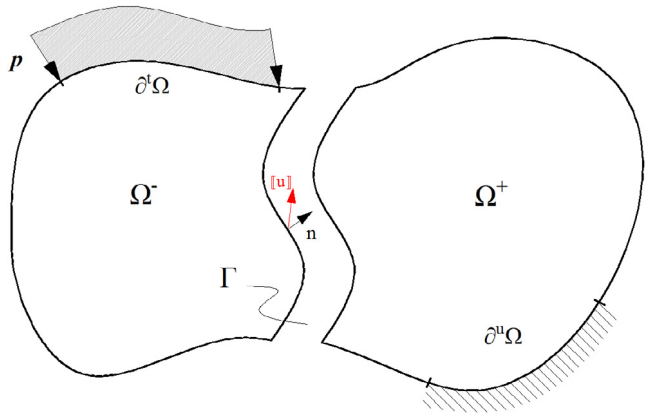

Fig. 1. Domain decomposition of Ω considering a cohesive crack Γ.

Furthermore, in the definition of the potential $\mathscr{L}^{\mathcal{F}}$, given by Eq. (2), Ψ is the cohesive energy density over the fracture Γ, defined as follows (see also [54]):

$$\begin{aligned} &\Psi(\boldsymbol{\delta},\kappa) = \boldsymbol{I}_{\mathbb{R}^+}(\delta_n) + \psi(\delta_{eq},\kappa) \quad with \quad \psi : \mathbb{R}^+ \to \mathbb{R}, \\ &\kappa(t) = \sup_{t'<t^*} \delta_{eq}(t'), \end{aligned} \tag{4}$$

where κ is an irreversibility internal variable in the crack, ψ represents the cohesive potential, $\boldsymbol{\delta}$ is a supplementary variable introduced latter, $\delta_n = \boldsymbol{\delta}\cdot\boldsymbol{n}$ is the projection of the supplementary variable on vector $\boldsymbol{n}$, $\delta_{eq} = \sqrt{\boldsymbol{\delta}\cdot\boldsymbol{\delta}}$ is the equivalent displacement jump and $\boldsymbol{I}_{\mathbb{R}^+}$ is an indicator function that is introduced to avoid penetration between crack lips. The irreversible variable κ introduced to control the crack opening/closure is defined as:

$$\kappa(t) := \sup_{t'<t^*} \delta_{eq}(t'); \tag{5}$$

where t^* is the actual time.

The functional $\mathscr{L}^{\boldsymbol{u}}$ presented in Eq. (1) is reformulated with an augmented Lagrangian method leading to a three fields equations system. Then, a coordination–decomposition method proposed in [55] decompose the equation in two problems, a global one corresponding to a linear form and a family of local problems in collocation points that are coordinated by the Lagrange multiplier field. The supplementary variable $\boldsymbol{\delta}$, restricted by the condition $[\![\boldsymbol{u}]\!] - \boldsymbol{\delta} = 0$, is introduced. The mechanical problem is therefore expressed as:

$$\begin{cases} \min\limits_{(\boldsymbol{u},\boldsymbol{\delta})\in\mathscr{V}\times\mathscr{X}} \mathscr{L}^{\mathcal{B}}(\boldsymbol{u}) + \mathscr{L}^{\mathcal{F}}(\boldsymbol{\delta}) \\ subjected \ \ to \ \ [\![\boldsymbol{u}]\!] - \boldsymbol{\delta} = 0. \end{cases} \tag{6}$$

The augmented Lagrangian $\mathscr{L} : \mathscr{V}\times\mathscr{W}\times\mathscr{X} \to \boldsymbol{R}$ associated to problem (6) is:

$$\mathscr{L}(\boldsymbol{u};\lambda;\boldsymbol{\delta}) = \mathscr{L}^{\mathcal{B}}_{\gamma}(\boldsymbol{u};\boldsymbol{\delta}) + \mathscr{L}^{\mathcal{F}}(\boldsymbol{\delta}) + \mathscr{L}^{\mathcal{C}}(\boldsymbol{u};\boldsymbol{\delta};\lambda), \tag{7}$$

where:

$$\begin{aligned} &\mathscr{L}^{\mathcal{B}}_{\gamma}(\boldsymbol{u},\boldsymbol{\delta}) = \mathscr{L}^{\mathcal{B}}(\boldsymbol{u}) + \int_{\Gamma} \frac{\gamma}{2}([\![\boldsymbol{u}]\!] - \boldsymbol{\delta})^2 \, d\Gamma, \\ &\mathscr{L}^{\mathcal{C}}(\boldsymbol{u};\boldsymbol{\delta},\lambda) = \int_{\Gamma} \lambda\cdot([\![\boldsymbol{u}]\!] - \boldsymbol{\delta}) \, d\Gamma. \end{aligned} \tag{8}$$

The second term in Eq. (7), where the cohesive energy density Ψ is immersed, now depends on the supplementary variable controlled in the third term by the Lagrangian field λ. This field fix in a weak sense the condition $[\![\boldsymbol{u}]\!] - \boldsymbol{\delta} = 0$ in Γ. The Lagrange multipliers can be interpreted as the traction over the fracture as $\lambda = -\boldsymbol{\sigma}\cdot\boldsymbol{n}$, as is shown in [49]. The penalization functional (with parameter $\gamma \in \Re^+$), is introduced in Eq. (8). With the coordination–decomposition method, the supplementary variable can be obtained as a algebraic function of the displacement field $\boldsymbol{u}$ and the Lagrangian field λ particularized in collocation points. The functional minimization problem presented in Eq. (6) turns to a saddle point problem, that can be expressed as: *For some $\gamma \in \mathbb{R}^+$, find $(\boldsymbol{u};\lambda) \in \mathscr{V}\times\mathscr{W}$ such that:*

$$\begin{aligned} \mathscr{G}_1(\boldsymbol{u};\boldsymbol{\delta};\lambda) = &\int_{\Omega\setminus\Gamma} \boldsymbol{\sigma}(x,t) : \nabla^s\delta\boldsymbol{u}(x,t) \, d\Omega \\ &+ \int_{\Gamma} [\lambda + \gamma([\![\boldsymbol{u}]\!] - \boldsymbol{\delta})]\cdot[\![\delta\boldsymbol{u}]\!] \, d\Gamma \\ &- \int_{\partial^t\Omega} \boldsymbol{p}(x,t)\cdot\delta\boldsymbol{u} \, d\partial^t\Omega - \int_{\Omega\setminus\Gamma} \boldsymbol{b}(x)\cdot\delta\boldsymbol{u} \, d\Omega = 0, \\ &\forall\delta\boldsymbol{u}\in\mathscr{V}, \\ \mathscr{G}_2(\boldsymbol{u};\boldsymbol{\delta};\lambda) = &\int_{\Gamma} ([\![\boldsymbol{u}]\!] - \boldsymbol{\delta})\cdot\delta\lambda \, d\Gamma = 0, \quad \forall\delta\lambda\in\mathscr{W}, \end{aligned} \tag{9}$$

with $\boldsymbol{\delta}(\boldsymbol{u};\lambda) \in \ker\{\partial_{\delta}\Psi - \lambda - \gamma([\![\boldsymbol{u}]\!] - \boldsymbol{\delta})\}$ where $\boldsymbol{u}$ and λ are fixed in collocation points. The space of kinematically admissible displacement variations for $\delta\boldsymbol{u}$ is denoted as $\mathscr{V}$ and $\mathscr{W}$ is the space of kinematically admissible variations of Lagrange multipliers $\delta\lambda$, given by:

$$\begin{aligned} &\mathscr{V}(\Omega\setminus\Gamma) = \left\{\boldsymbol{\phi}\in\mathbf{H}^1 \ \wedge \ [\![\boldsymbol{\phi}]\!]\in\mathbf{H}^{\frac{1}{2}} : \boldsymbol{\phi}|_{\partial^u\Omega} = 0\right\}, \\ &\mathscr{W}(\Omega\setminus\Gamma) = \left\{\boldsymbol{\phi}|\boldsymbol{\phi}\in\mathbf{H}^{-\frac{1}{2}}\right\}. \end{aligned} \tag{10}$$

In the proposed multi-scale approach the equilibrium equations (9) are used to simulate cohesive fracture in both scales were presented in (9), and now the basic equations are known to state the proposed multi-scale scheme. Note that the choice of the space of Lagrange multipliers is not straightforward. The discrete spaces used in the numerical tests fulfil the inf–sup condition [49,56]. A rigorous proof of this aspect is beyond the scope of the present paper. Conditions of discrete spaces to fulfil stability conditions can be found in [57,58].

2.2. Traction separation law

The linear softening cohesive zone model proposed in [59] with crumpling and unloading stages showed in Fig. 2 is used in this paper.

The potential is defined as follow:

$$\psi(\delta_{eq}) = \begin{cases} G_c\dfrac{\delta_{eq}}{\delta_c}\left(2 - \dfrac{\delta_{eq}}{\delta_c}\right), & if \ \ \delta_{eq} \le \delta_c \\ G_c, & if \ \ \delta_{eq} > \delta_c, \end{cases} \tag{11}$$

where $G_c = \frac{1}{2}\sigma_c\delta_c$ is the fracture energy and σ_c the critical tension.

3. Semi-concurrent multi-scale formulation based in an hybrid injection

The proposed model is split in two stages: the first one for a stable material behaviour, based on a classic formulation is presented in Section 3.1 and the latter, the proposed formulation for the unstable or softening regime is described in Section 3.2. The activation of the unstable regime is detected using the acoustic tensor [60,61]. The proposed multi-scale formulation is based on two fundamentals axioms: (A1) the kinematical admissibility that both scales kinematics have to meet [30] and (A2) the multiscale principle of virtual power [30] or Hill–Mandel principle [62,63]. From these fundamental axioms, two consequences are obtained: (C1) The homogenization formula for dual variable and (C2) the equilibrium problem at the micro scale. In the following, the sub-index μ is used to denote the variables or parameters associated to the micro-scale, i.e. $(\bullet)_{\mu}$ is the variable $(\bullet)$ associated to the **RVE**.

3.1. Multi-scale formulation for a stable regime

3.1.1. (A1) Axiom 1. Kinematical assumption in the scale transition. Stable regime

The multi-scale constitutive formulation is based on the assumption that the strain tensor $\boldsymbol{\varepsilon}$ at a macro-continuum point $\boldsymbol{x}$ is the volume

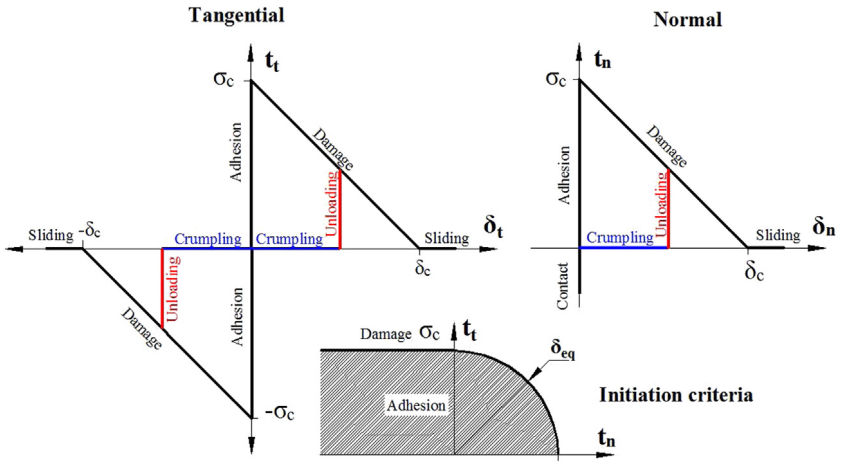

Fig. 2. Traction separation law based in [59] for $\delta_n > 0$. (a) Tangential law (b) Normal law (c) Initiation criteria.

average of the micro-continuum strain field, $\boldsymbol{\varepsilon}_\mu$, over the RVE associated with $\boldsymbol{x}$. Considering the symmetric part of the gradient of microscopic displacement field $\boldsymbol{u}_\mu$, denoted as $\nabla^s_{\mathbf{y}}\, \boldsymbol{u}_\mu$, for the strain field:

$$d\boldsymbol{\varepsilon}(\boldsymbol{x},t) = \frac{1}{|\Omega_\mu|}\int_{\Omega_\mu} d\boldsymbol{\varepsilon}_\mu(\mathbf{y},t)\, d\Omega_\mu + \frac{1}{|\Omega_\mu|}\int_{\Gamma_\mu} [\![d\boldsymbol{u}_\mu]\!]_{\mathbf{y}} \otimes^s \boldsymbol{n}_\mu \, d\Gamma_\mu = \\ = \frac{1}{|\Omega_\mu|}\int_{\Omega_\mu} \nabla^s_{\mathbf{y}}\, d\boldsymbol{u}_\mu \, d\Omega_\mu + \frac{1}{|\Omega_\mu|}\int_{\Gamma_\mu} [\![d\boldsymbol{u}_\mu]\!]_{\mathbf{y}} \otimes^s \boldsymbol{n}_\mu \, d\Gamma_\mu, \tag{12}$$

where $|\Omega_\mu|$ is the volume of the RVE, $\boldsymbol{x}$ and $\mathbf{y}$ denote the coordinates systems of the macro- a micro-scale, respectively, $[\![\bullet]\!]_{\mathbf{y}} = (\bullet)|_{\Gamma^+_\mu} - (\bullet)|_{\Gamma^-_\mu}$ represents the jump of $(\bullet)$ over the crack Γ_μ and $\boldsymbol{n}_\mu$ denotes the normal vector to the crack Γ_μ. The displacement fields $d\boldsymbol{u}_\mu$ that satisfy Eq. (12), can be said to be a kinematically admissible if $d\boldsymbol{u}_\mu \in \mathscr{U}^*_\mu$ with:

$$\mathscr{U}^*_\mu := \left\{ \boldsymbol{\varphi} \in \boldsymbol{H}^1(\Omega_\mu) \mid d\boldsymbol{\varepsilon}(\boldsymbol{x},t) = \frac{1}{|\Omega_\mu|}\int_{\Omega_\mu} \nabla^s_{\mathbf{y}}\, \boldsymbol{\varphi}\, d\Omega_\mu \right. \\ \left. + \frac{1}{|\Omega_\mu|}\int_{\Gamma_\mu} [\![\boldsymbol{\varphi}]\!]_{\mathbf{y}} \otimes^s \boldsymbol{n}_\mu \, d\Gamma_\mu \right\}, \tag{13}$$

being $\mathscr{U}^*_\mu$ the set of kinematically admissible micro displacements. If displacement jumps are considered in the RVE, the first integral in Eq. (12) should be evaluated in two or more parts separated by the discontinuities. Applying Green's theorem in the first term of Eq. (12) and considering the presence of displacement jumps in the RVE (Fig. 3):

$$d\boldsymbol{\varepsilon}(\boldsymbol{x},t) = \frac{1}{|\Omega_\mu|}\left[\int_{\partial\Omega_\mu} d\boldsymbol{u}_\mu \otimes^s \boldsymbol{\nu}\, d\partial\Omega_\mu + \int_{\Gamma^+_\mu} d\boldsymbol{u}^+_\mu \otimes^s \boldsymbol{n}^+_\mu \, d\Gamma^+_\mu \right. \\ \left. + \int_{\Gamma^-_\mu} d\boldsymbol{u}^-_\mu \otimes^s \boldsymbol{n}^-_\mu \, d\Gamma^-_\mu + \int_{\Gamma_\mu} [\![d\boldsymbol{u}]\!]_{\mathbf{y}} \otimes^s \boldsymbol{n}_\mu \, d\Gamma_\mu \right], \tag{14}$$

where $\boldsymbol{\nu}$ is the outer normal vector of the RVE boundary $\partial\Omega_\mu$ and the unit vectors $\boldsymbol{n}^+_\mu$ and $\boldsymbol{n}^-_\mu$ are the fracture lips normal denoted as Γ^+_μ and Γ^-_μ. Considering $\boldsymbol{n}^+_\mu = -\boldsymbol{n}^-_\mu$, Eq. (14) can be rewritten as:

$$d\boldsymbol{\varepsilon}(\boldsymbol{x},t) = \frac{1}{|\Omega_\mu|}\left[\int_{\partial\Omega_\mu} d\boldsymbol{u}_\mu \otimes^s \boldsymbol{\nu}\, d\partial\Omega_\mu \right]. \tag{15}$$

Without loss of generality, $\boldsymbol{u}_\mu$ can be split into a sum of the macroscopic displacement field $\boldsymbol{u}$, the contribution provided by the macroscopic strain $\boldsymbol{\varepsilon}(\boldsymbol{x},t)$ and a fluctuation displacement field $\tilde{\boldsymbol{u}}_\mu$ [26,30,45]

$$d\boldsymbol{u}_\mu(\mathbf{y}) = d\boldsymbol{u} + d\boldsymbol{\varepsilon}\left(\mathbf{y} - \mathbf{y}_0\right) + d\tilde{\boldsymbol{u}}_\mu(\mathbf{y}) \Rightarrow [\![d\boldsymbol{u}_\mu]\!]_{\mathbf{y}} = [\![d\tilde{\boldsymbol{u}}_\mu]\!]_{\mathbf{y}}, \tag{16}$$

with

$$\mathbf{y}_0 = \frac{1}{|\Omega_\mu|}\int_{\Omega_\mu} \mathbf{y}\, d\Omega_\mu, \tag{17}$$

Consequently, the microscopic strain field is:

$$d\boldsymbol{\varepsilon}_\mu(\mathbf{y},t) = \nabla^s_{\mathbf{y}}\, d\boldsymbol{u}_\mu(\mathbf{y}) = d\boldsymbol{\varepsilon}(\boldsymbol{x},t) + \nabla^s_{\mathbf{y}}\, d\tilde{\boldsymbol{u}}_\mu(\mathbf{y}). \tag{18}$$

Then, replacing the last equation in Eq. (15), constraint (12) only depends on the fluctuation field and yields to:

$$\int_{\partial\Omega_\mu} d\tilde{\boldsymbol{u}}_\mu \otimes^s \boldsymbol{\nu}\, d\partial\Omega_\mu = 0. \tag{19}$$

In order to remove rigid modes, the following constraint on the microscopic displacement field $\tilde{\boldsymbol{u}}_\mu$ is assumed:

$$d\boldsymbol{u}(\boldsymbol{x},t) = \frac{1}{|\Omega_\mu|}\left[\int_{\Omega_\mu} d\boldsymbol{u}_\mu(\mathbf{y},t)\, d\Omega_\mu \right]. \tag{20}$$

Combining Eq. (20) with (16), an additional constraint is obtained for the fluctuation displacement field:

$$\int_{\Omega_\mu} d\tilde{\boldsymbol{u}}_\mu(\mathbf{y},t)\, d\Omega_\mu = 0. \tag{21}$$

Hence, the set of kinematically admissible micro displacements $\mathscr{U}^*_\mu$ can be redefined as the space of kinematically admissible micro displacement fluctuations i.e. $\tilde{\boldsymbol{u}}_\mu \in \tilde{\mathscr{V}}_\mu$ with:

$$\tilde{\mathscr{V}}_\mu := \left\{ \boldsymbol{\varphi} \in \boldsymbol{H}^1(\Omega_\mu) \mid \int_{\Omega_\mu} \boldsymbol{\varphi}\, d\Omega_\mu = 0 \;\; and \;\; \int_{\partial\Omega_\mu} \boldsymbol{\varphi} \otimes^s \boldsymbol{\nu}\, d\partial\Omega_\mu \right\}. \tag{22}$$

Observation 3.1. *The space of kinematically admissible micro displacements admits, at least, three sub spaces that satisfy the kinematic admissibility: the Taylor space $\mathscr{V}^{Taylor}_\mu$, the linear space $\mathscr{V}^{Lineal}_\mu$ and the periodic space $\mathscr{V}^{Per}_\mu$* [26,30,45,46]:

$$\mathscr{V}^{Taylor}_\mu \subseteq \mathscr{V}^{Lineal}_\mu \subseteq \mathscr{V}^{Per}_\mu \subseteq \mathscr{V}^{Min}_\mu \equiv \tilde{\mathscr{V}}_\mu. \tag{23}$$

3.1.2. (A2) Axiom 2. Principle of Multiscale virtual power and its variational consequences. Stable regime

The physical bridging between macro and micro scales is provided by the principle of Multiscale virtual power [30], the extension of the Hill–Mandel principle [62,63]. For this case, the principle is written as:

$$\boldsymbol{\sigma} \cdot \nabla^s_{\boldsymbol{x}}\, \delta\boldsymbol{u} = \frac{1}{|\Omega_\mu|}\left[\int_{\Omega_\mu} \boldsymbol{\sigma}_\mu \cdot \nabla^s_{\mathbf{y}}\, \delta\boldsymbol{u}_\mu \, d\Omega_\mu + \int_{\Gamma_\mu} \lambda_\mu \cdot [\![\delta\boldsymbol{u}_\mu]\!]_{\mathbf{y}} \, d\Gamma_\mu \right] \\ = \frac{1}{|\Omega_\mu|}\left[\int_{\Omega_\mu} \boldsymbol{\sigma}_\mu \cdot \left(\nabla^s_{\boldsymbol{x}}\, \delta\boldsymbol{u} + \nabla^s_{\mathbf{y}}\, \delta\tilde{\boldsymbol{u}}_\mu \right) d\Omega_\mu \right. \\ \left. + \int_{\Gamma_\mu} \lambda_\mu \cdot [\![\delta\tilde{\boldsymbol{u}}_\mu]\!]_{\mathbf{y}} \, d\Gamma_\mu \right], \quad \forall \left(\delta\boldsymbol{u}, \delta\tilde{\boldsymbol{u}}_\mu\right) \in \mathscr{V} \times \tilde{\mathscr{V}}_\mu, \tag{24}$$

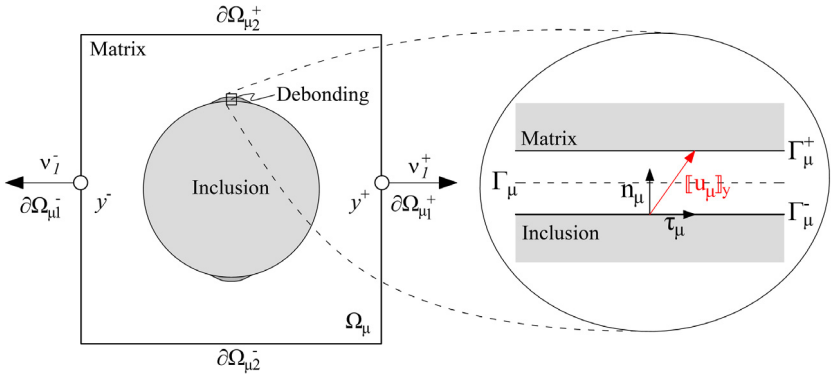

Fig. 3. Micro-continuum (RVE) with a discontinuity in the **RVE** displacement field.

where the second term is the contribution of the discontinuity between the materials, being λ_μ the projection of the micro stress field $\boldsymbol{\sigma}_\mu$ over the normal $\boldsymbol{n}_\mu$ to the discontinuity Γ_μ. Two consequences can be obtained from Eq. (24): (C1) the mechanical equilibrium equations of the micro scale problem and (C2) the homogenization formula for the Cauchy stress.

3.1.3. (C1) Consequence 1. Micro mechanical equilibrium problem. Stable regime

Considering $\nabla^s_{\boldsymbol{x}}\ \delta\boldsymbol{u} = 0$ in Eq. (24), the mechanical equilibrium equations for the micro-scale including debonding are obtained: *Find* $\tilde{\boldsymbol{u}}_\mu \in \tilde{\mathscr{V}}_\mu$ *such that*

$$\int_{\Omega_\mu} \boldsymbol{\sigma}_\mu \cdot \nabla^s_{\boldsymbol{y}}\ \delta\tilde{\boldsymbol{u}}_\mu\ d\Omega_\mu + \int_{\Gamma_\mu} \lambda_\mu \cdot [\![\ \delta\tilde{\boldsymbol{u}}_\mu]\!]_{\boldsymbol{y}}\ d\Gamma_\mu = 0,\quad \forall\delta\tilde{\boldsymbol{u}}_\mu \in \tilde{\mathscr{V}}_\mu. \tag{25}$$

3.1.4. (C2) Consequence 2. Characterization of the macroscopic stress. Stable regime

Considering $\delta\tilde{\boldsymbol{u}}_\mu = 0$ in Eq. (24), the macroscopic stress state $\boldsymbol{\sigma}(\boldsymbol{x},t)$ can be obtained as:

$$\boldsymbol{\sigma}(\boldsymbol{x},t) = \frac{1}{|\Omega_\mu|}\int_{\Omega_\mu} \boldsymbol{\sigma}_\mu(\boldsymbol{y},t)\ d\Omega_\mu \tag{26}$$

All the elements for a consistent multi scale model within a stable regime, considering discontinuities in the RVE were exposed.

Observation 3.2. *The term corresponding to the fracture equilibrium in the micro mechanical equilibrium equation (25) is calculated considering the interface stresses as an additional unknown variable. The RVE problem is: For some* $\gamma \in \mathbb{R}^+$, *find* $(\tilde{\boldsymbol{u}}_\mu, \lambda_\mu) \in \tilde{\mathscr{V}}_\mu \times \mathscr{W}_\mu$ *such that* $\forall\delta\tilde{\boldsymbol{u}}_\mu \in \tilde{\mathscr{V}}_\mu$ *and* $\forall\delta\lambda_\mu \in \mathscr{W}_\mu$, *the following equations are fulfilled:*

$$\begin{aligned}
&\int_{\Omega_\mu} \boldsymbol{\sigma}_\mu \cdot \nabla^s_{\boldsymbol{y}}\ \delta\tilde{\boldsymbol{u}}_\mu\ d\Omega_\mu + \int_{\Gamma_\mu} \left(\lambda_\mu + \gamma\left([\![\ \tilde{\boldsymbol{u}}_\mu]\!]_{\boldsymbol{y}} - \boldsymbol{\delta}_\mu\right)\right) \cdot [\![\ \delta\tilde{\boldsymbol{u}}_\mu]\!]_{\boldsymbol{y}}\ d\Gamma_\mu = 0,\\
&\quad \forall\delta\tilde{\boldsymbol{u}}_\mu \in \tilde{\mathscr{V}}_\mu,\\
&\int_{\Gamma_\mu} \left([\![\ \tilde{\boldsymbol{u}}_\mu]\!]_{\boldsymbol{y}} - \boldsymbol{\delta}_\mu\right) \cdot\ \delta\lambda_\mu\ d\Gamma_\mu = 0,\quad \forall\delta\tilde{\lambda}_\mu \in \mathscr{W}_\mu,
\end{aligned} \tag{27}$$

with

$$\mathscr{W}_\mu\left(\Omega_\mu \setminus \Gamma_\mu\right) = \left\{\delta\lambda_\mu \mid \delta\lambda_\mu \in \mathbf{H}^{-\frac{1}{2}}\right\}. \tag{28}$$

space of kinematically admissible surface traction variations, γ *is a penalty parameter and* $\boldsymbol{\delta}_\mu$ *is a supplementary variable to control the constitutive behaviour in the fracture* Γ_μ.

3.1.5. Macroscopic consistent constitutive tangent tensor

Once the micro-mechanical problem is solved, the macro-scale constitutive tangent tensor which describes the behaviour of the adopted **RVE** is required, for the implementation within a conventional Newton–Raphson scheme. This tensor can be also used to study the lost of ellipticity and the initiation of a failure mechanisms in the macro structure. According to the traditional definition of the tangent operator [45]:

$$\mathbb{C}\left(\boldsymbol{\epsilon}^t\right) = \left.\frac{D\boldsymbol{\sigma}}{D\boldsymbol{\varepsilon}}\right|_{\boldsymbol{\varepsilon}} = \left.\frac{Dd\boldsymbol{\sigma}}{Dd\boldsymbol{\varepsilon}}\right|_{\boldsymbol{\varepsilon}}, \tag{29}$$

where $\frac{D(\bullet)}{D\boldsymbol{\varepsilon}}$ represents the total derivative with respect to the macro strain $\boldsymbol{\varepsilon}$. Considering the Eqs. (18) and (25) the following equation is obtained:

$$\begin{aligned}
\mathbb{C} = \left.\frac{Dd\boldsymbol{\sigma}}{Dd\boldsymbol{\varepsilon}}\right|_{\boldsymbol{\varepsilon}} &= \frac{1}{|\Omega_\mu|}\int_{\Omega_\mu} \left.\frac{Dd\boldsymbol{\sigma}_\mu}{Dd\boldsymbol{\varepsilon}}\right|_{\boldsymbol{\varepsilon}} d\Omega_\mu\\
&= \frac{1}{|\Omega_\mu|}\int_{\Omega_\mu} \left[\left.\frac{\partial d\boldsymbol{\sigma}_\mu}{\partial d\boldsymbol{\varepsilon}_\mu}\right|_{\boldsymbol{\varepsilon}} + \left.\frac{\partial d\boldsymbol{\sigma}_\mu}{\partial d\boldsymbol{\varepsilon}_\mu}\right|_{\boldsymbol{\varepsilon}} :\ \left.\frac{\partial d\tilde{\boldsymbol{\varepsilon}}_\mu}{\partial d\boldsymbol{\varepsilon}}\right|_{\boldsymbol{\varepsilon}}\right] d\Omega_\mu\\
&= \frac{1}{|\Omega_\mu|}\int_{\Omega_\mu} \mathbb{C}_\mu\ d\Omega_\mu + \frac{1}{|\Omega_\mu|}\int_{\Omega_\mu} \mathbb{C}_\mu :\ \left.\frac{\partial d\tilde{\boldsymbol{\varepsilon}}_\mu}{\partial d\boldsymbol{\varepsilon}}\right|_{\boldsymbol{\varepsilon}} d\Omega_\mu\\
&= \bar{\mathbb{C}} + \tilde{\mathbb{C}},
\end{aligned} \tag{30}$$

where $\mathbb{C}_\mu$ is the constitutive tangent tensor at the micro-scale, which depends on the adopted constitutive functional $\mathscr{F}_\mu\left(\boldsymbol{\varepsilon}^t_\mu\right)$ in each point $\boldsymbol{y}$ of the RVE. The macroscopic constitutive tensor $\mathbb{C}$ is expressed in terms of the summation of a component called Taylor $\bar{\mathbb{C}}$, and a contribution of the fluctuation field $\tilde{\mathbb{C}}$. It is clear that the displacement jumps in the **RVE** has not any influence in the first term. With the directional derivative of the equilibrium equation (25) in the $\boldsymbol{\varepsilon}_{ij}$ direction and considering the possibility of displacement jumps s.t. $\exists\boldsymbol{y} \in \Omega_\mu \mid [\![\boldsymbol{u}_\mu(\boldsymbol{y})]\!]_{\boldsymbol{y}} \neq 0$, the following equation is obtained:

$$\begin{aligned}
&\int_{\Gamma_\mu} \frac{\partial\lambda_\mu\left([\![\ \tilde{\boldsymbol{u}}_\mu]\!]_{\boldsymbol{y}}\right)}{\partial\boldsymbol{\varepsilon}_{ij}}\ [\![\ \delta\tilde{\boldsymbol{u}}_\mu]\!]_{\boldsymbol{y}}\ d\Gamma_\mu + \int_{\Omega_\mu} \mathbb{C}^T_\mu \cdot \left(\boldsymbol{e}_i \otimes^s \boldsymbol{e}_j\right) \cdot \nabla^s_{\boldsymbol{y}}\ \delta\tilde{\boldsymbol{u}}_\mu\ d\Omega_\mu +\\
&\quad + \int_{\Omega_\mu} \mathbb{C}^T_\mu \cdot \left(\nabla^s_{\boldsymbol{y}}\left[D_\varepsilon\right]_{ij}\right) \cdot \nabla^s_{\boldsymbol{y}}\ \delta\tilde{\boldsymbol{u}}_\mu\ d\Omega_\mu = 0,\quad \forall\delta\tilde{\boldsymbol{u}}_\mu \in \tilde{\mathscr{V}}_\mu.
\end{aligned} \tag{31}$$

The first term can be rewritten as:

$$\begin{aligned}
&\int_{\Gamma_\mu} \frac{\partial\lambda_\mu}{\partial[\![\tilde{\boldsymbol{u}}_\mu]\!]_{\boldsymbol{y}}} \frac{\partial[\![\tilde{\boldsymbol{u}}_\mu]\!]_{\boldsymbol{y}}}{\partial\boldsymbol{\varepsilon}_{ij}}\ [\![\ \delta\tilde{\boldsymbol{u}}_\mu]\!]_{\boldsymbol{y}}\ d\Gamma_\mu + \int_{\Omega_\mu} \mathbb{C}^T_\mu \cdot \left(\boldsymbol{e}_i \otimes^s \boldsymbol{e}_j\right) \cdot \nabla^s_{\boldsymbol{y}}\ \delta\tilde{\boldsymbol{u}}_\mu\ d\Omega_\mu +\\
&\quad + \int_{\Omega_\mu} \mathbb{C}^T_\mu \cdot \left(\nabla^s_{\boldsymbol{y}}\left[D_\varepsilon\right]_{ij}\right) \cdot \nabla^s_{\boldsymbol{y}}\ \delta\tilde{\boldsymbol{u}}_\mu\ d\Omega_\mu = 0,\quad \forall\delta\tilde{\boldsymbol{u}}_\mu \in \tilde{\mathscr{V}}_\mu,
\end{aligned} \tag{32}$$

with $\left[D_\varepsilon\right]_{ij} = \frac{\partial\tilde{\boldsymbol{u}}_\mu}{\partial\boldsymbol{\varepsilon}_{ij}}$. The term $\frac{\partial\lambda_\mu}{\partial[\![\tilde{\boldsymbol{u}}_\mu]\!]_{\boldsymbol{y}}}$ represents the tangent constitutive matrix (or tensor) corresponding to the traction separation law in the fracture domain. In this way, a set of equations for $\frac{\partial\tilde{\boldsymbol{u}}_\mu}{\partial\boldsymbol{\varepsilon}_{ij}}$ (in two dimension $i,j = 1,2$ and in three dimension $i,j = 1,2,3$), is obtained. Once the equations system is solved, the fluctuation constitutive tensor $\tilde{\mathbb{C}}$ can be written as:

$$\tilde{\mathbb{C}} = \frac{1}{|\Omega_\mu|}\int_{\Omega_\mu} \mathbb{C}^T_\mu \left(\nabla^s_{\boldsymbol{y}}\left[D_\varepsilon\right]_{kl}\right)_{ij}\ \boldsymbol{e}_i \otimes^s \boldsymbol{e}_j \otimes^s \boldsymbol{e}_k \otimes^s \boldsymbol{e}_l\ d\Omega_\mu. \tag{33}$$

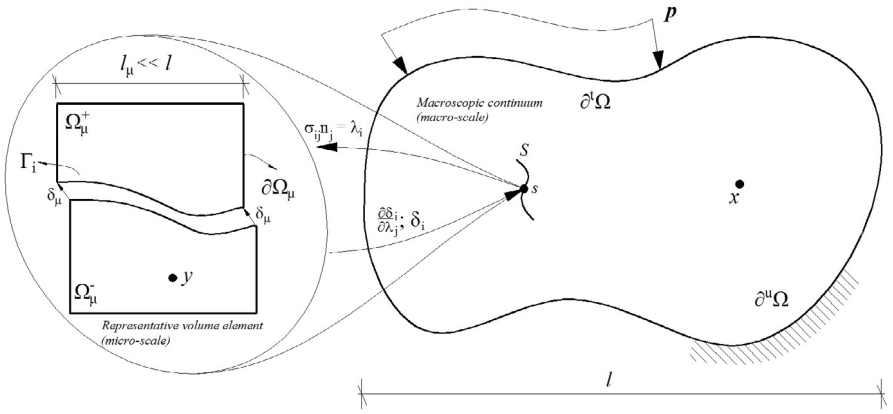

Fig. 4. Macroscopic continuous with a discontinuity and its associated **RVE**.

Introducing the solution of the system (32) in Eq. (33), and considering Eq. (30), the tangent constitutive tensor $\mathbb{C}$ is obtained.

3.2. Multi-scale model for unstable or softening regime

For the determination of the unstable regime, the criterion based on the acoustic tensor analysis, see [64], was considered. Therefore, the unstable stage is reached when the determinant of the acoustic tensor becomes null:

$$\det\left(\mathbb{Q}\left(\boldsymbol{n}\right)\right) = \det\left(\boldsymbol{n}\cdot\mathbb{C}\cdot\boldsymbol{n}\right) = 0, \quad for \quad t = t_N \quad , \tag{34}$$

where $\boldsymbol{n}$ is the normal vector of the discontinuity $\mathcal{S}$ at the macro-scale, see Fig. 4.

The phenomenological constitutive response presented in Section 2.2 is now considered at the micro-scale level for the fracture domain Γ_μ in the **RVE**, the jump vector $\boldsymbol{\delta}_\mu$ is defined in the following sense:

$$\boldsymbol{\delta}_\mu := \mathscr{S}_\mu\left(\lambda_\mu^t\right) = \mathscr{S}_\mu\left(\lambda_\mu^{t-dt}, d\lambda_\mu\right), \tag{35}$$

where $\mathscr{S}_\mu$ is a generic constitutive functional and $(\bullet)^t$ is the history of the variable over the time t.

In time t_L, a localized domain $\Gamma_\mu^L \subset \Gamma_\mu$ appears in the micro-scale. Following Ref. [31], these domain is defined as:

$$\Gamma_\mu^L = \left\{\cup\Gamma_\mu^i \in \Omega_\mu \;\; such \;\; that \;\; \left(\left[\!\left[d\boldsymbol{u}_\mu^i\right]\!\right]_{\boldsymbol{y}} \otimes {}^s\boldsymbol{n}_\mu^i\right)\cdot\left(d\boldsymbol{\gamma}\otimes{}^s\boldsymbol{n}\right) > 0, \right.$$
$$\left. with\; i = 1,\ldots,n_T\right\}, \tag{36}$$

where Γ_μ^i are the crack elements in the **RVE** subjected to an incremental discontinuity $\left[\!\left[d\boldsymbol{u}_\mu^i\right]\!\right]_{\boldsymbol{y}}$, $d\boldsymbol{\gamma}$ is the initial direction of the macroscopic discontinuity and n_T is the total number of discontinuities. The set presented in Eq. (36), represents the set of fractured elements that has an opening inertia equal to the inertia of the macro-scale fracture. This sub domain $\Gamma_\mu^L \subseteq \Gamma_\mu$ is fixed for $t > t_L$.

3.2.1. (A1) Equivalent kinematical assumption in the scale transition. Unstable regime

For the points at the macroscale undergoing an unstable regime, the kinematic in the scale transition assumption is expressed in terms of the Lagrange multipliers field λ (of physically, the surface traction in the discontinuity with normal $\boldsymbol{n}$), stated as follows

$$d\lambda = -d\boldsymbol{\sigma}\cdot\boldsymbol{n} = \frac{1}{|\boldsymbol{n}_m|}\int_{\Gamma_\mu^L} d\lambda_\mu^L\, d\Gamma_\mu^L = \frac{1}{|\boldsymbol{n}_m|}\int_{\Gamma_\mu^L} d\boldsymbol{\sigma}_\mu\cdot\boldsymbol{n}_\mu^L\, d\Gamma_\mu^L, \tag{37}$$

$$d\lambda_\mu^L = \frac{|\boldsymbol{n}_m|}{|\Gamma_\mu^L|}\, d\lambda + d\tilde{\lambda_\mu} = -\frac{|\boldsymbol{n}_m|}{|\Gamma_\mu^L|}\, d\boldsymbol{\sigma}\cdot\boldsymbol{n} + d\tilde{\lambda}_\mu^L. \tag{38}$$

where

$$\boldsymbol{n}_m = \int_{\Gamma_\mu^L} \boldsymbol{n}_\mu^L\, d\Gamma_\mu^L, \tag{39}$$

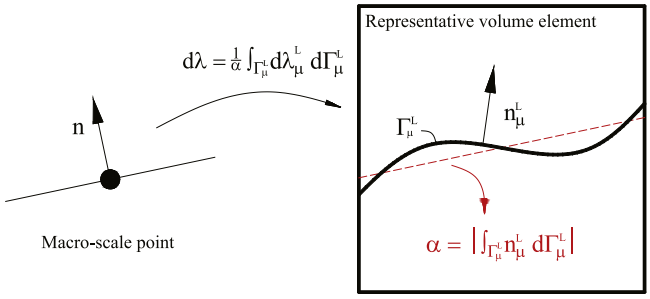

Fig. 5. Kinematics in the scale transition. A schematic interpretation.

is the mean normal, Γ_μ^L is a fracture subset of Γ_μ where the localization is expressed in the **RVE** and $\boldsymbol{\sigma}_\mu$ is the stress field of the micro-scale. Note that the last term in (38), $d\tilde{\lambda_\mu^L}$, represents the traction fluctuations over Γ_μ^L. It should be observed that in the mixed formulation, the kinematical assumption in the scale transition is actually an equilibrium assumption and it is call kinematical only to preserve the analogy with classical multi-scale approach. Replacing Eq. (38) in (37)

$$\begin{aligned} -d\boldsymbol{\sigma}\cdot\boldsymbol{n} &= \frac{1}{|\boldsymbol{n}_m|}\int_{\Gamma_\mu^L}\left(-\frac{|\boldsymbol{n}_m|}{|\Gamma_\mu^L|}d\boldsymbol{\sigma}\cdot\boldsymbol{n} + d\tilde{\lambda_\mu^L}\right) d\Gamma_\mu^L, \\ &= -\frac{1}{|\Gamma_\mu^L|}\int_{\Gamma_\mu^L} d\boldsymbol{\sigma}\cdot\boldsymbol{n}\, d\Gamma_\mu^L + \frac{1}{|\boldsymbol{n}_m|}\int_{\Gamma_\mu} d\tilde{\lambda_\mu^L}\, d\Gamma_\mu^L, \\ &= -d\boldsymbol{\sigma}\cdot\boldsymbol{n}\,\frac{1}{|\Gamma_\mu^L|}\int_{\Gamma_\mu^L} d\Gamma_\mu^L + \frac{1}{|\boldsymbol{n}_m|}\int_{\Gamma_\mu^L} d\tilde{\lambda_\mu^L}\, d\Gamma_\mu^L, \end{aligned} \tag{40}$$

where the incremental traction field in the localization $d\lambda_\mu^L$ is related with the tension in the macro scale fracture $-d\boldsymbol{\sigma}\cdot\boldsymbol{n}$, giving a final condition

$$\int_{\Gamma_\mu^L} d\tilde{\lambda_\mu^L}\, d\Gamma_\mu^L = 0, \quad \vee \quad \int_{\Gamma_\mu^L} d\tilde{\boldsymbol{\sigma}_\mu}\cdot\boldsymbol{n}_\mu^L\, d\Gamma_\mu^L = 0. \tag{41}$$

Finally, the space of kinematically admissible traction fluctuations in the localization is:

$$\tilde{\mathscr{W}}_\mu^{\Gamma_\mu^L}\left(\Omega_\mu\setminus\Gamma_\mu\right) := \left\{\boldsymbol{\varphi}|\boldsymbol{\varphi}\in\mathbf{H}^{-\frac{1}{2}} \;\wedge\; \int_{\Gamma_\mu^L}\boldsymbol{\varphi}\, d\Gamma_\mu^L = 0\right\}. \tag{42}$$

It can be observed in Fig. 5 that the mean-length $\alpha = |\boldsymbol{n}_m|$ of the localization Γ_μ^L is a length parameter that was introduced in the kinematic scale transition and it is analogous to that used in Ref. [31]. The parameter $\frac{|\boldsymbol{n}_m|}{|\Gamma_\mu^L|} \in (0,1]$ defined in Eq. (38) considers the torturous character of the localization in the **RVE**, being 1 for plane fractures and tending to zero for an infinitely tortuous crack path.

3.2.2. (A2) Principle of multi-scale virtual potential. Unstable regime

The physical consistency between both scales can be stated using the virtual potential balance. In the available multi-scales formulations, this consistency a-priori assumes the use of a single unknown field [31,46,47]. In this case in which a mixed approach is used to solve the problem at both scales, two unknown fields are involved. For this reason, the axiom starts from the potential in the macro scale $\Pi(\boldsymbol{u},\lambda)$ and the micro scale $\Pi_\mu(\boldsymbol{\varepsilon},\lambda,\tilde{\boldsymbol{u}}_\mu,\tilde{\lambda}_\mu)$.

Considering a point $\boldsymbol{s}\in\mathcal{S}$ belonging to the macro fracture, a potential can be stated as follows

$$\Pi(\boldsymbol{u},\lambda)=[\![\boldsymbol{u}]\!]\cdot\lambda\,, \tag{43}$$

and the total variation of the macro potential is

$$\delta\Pi(\boldsymbol{u},\lambda)=[\![\delta\boldsymbol{u}]\!]\cdot\lambda+[\![\boldsymbol{u}]\!]\cdot\delta\lambda. \tag{44}$$

Analogously to Axiom 1, the parameter $|\Gamma_\mu^L|$ representing the surface localization in the **RVE**, is introduced to formulate the micro-scale potential $\Pi_\mu(\boldsymbol{\varepsilon},\lambda,\tilde{\boldsymbol{u}}_\mu,\tilde{\lambda}_\mu)$. A penalization functional is introduced to maintain the consistency of the mathematical structure presented in Section 2, giving the following expression

$$\begin{aligned}&\Pi_\mu(\boldsymbol{\varepsilon},\lambda,\tilde{\boldsymbol{u}}_\mu,\tilde{\lambda}_\mu)\\&=\frac{1}{|\Gamma_\mu^L|}\left[\int_{\Omega_\mu}\boldsymbol{\sigma}_\mu\cdot\nabla^s\boldsymbol{u}_\mu\,d\Omega_\mu+\int_{\Gamma_\mu}\tilde{\lambda}_\mu\cdot\left([\![\boldsymbol{u}_\mu]\!]_{\mathbf{y}}-\boldsymbol{\delta}_\mu\right)\,d\Gamma_\mu+\right.\\&\quad+\int_{\Gamma_\mu}\frac{\gamma}{2}\left([\![\boldsymbol{u}_\mu]\!]_{\mathbf{y}}-\boldsymbol{\delta}_\mu\right)\cdot\left([\![\boldsymbol{u}_\mu]\!]_{\mathbf{y}}-\boldsymbol{\delta}_\mu\right)\,d\Gamma_\mu+\\&\quad\left.+\frac{|\boldsymbol{n}_m|}{|\Gamma_\mu^L|}\int_{\Gamma_\mu^L}\lambda\cdot[\![\boldsymbol{u}_\mu]\!]_{\mathbf{y}}\,d\Gamma_\mu^L\right],\end{aligned} \tag{45}$$

It should be observed that the last term of micro potential relates the traction in the macro crack with the jump field in the localization of the **RVE**, while the rest of cracks in the **RVE** $\Gamma_\mu\setminus\Gamma_\mu^L$ are only driven by the Lagrange multipliers fluctuation field. The total variation can be written as:

$$\delta\Pi_\mu(\boldsymbol{\varepsilon},\lambda,\tilde{\boldsymbol{u}}_\mu,\tilde{\lambda}_\mu)=\delta_\varepsilon\Pi_\mu+\delta_\lambda\Pi_\mu+\delta_{\tilde{\boldsymbol{u}}_\mu}\Pi_\mu+\delta_{\tilde{\lambda}_\mu}\Pi_\mu\,, \tag{46}$$

with

$$\delta_\varepsilon\Pi_\mu(\boldsymbol{\varepsilon},\lambda,\tilde{\boldsymbol{u}}_\mu,\tilde{\lambda}_\mu)=\frac{1}{|\Gamma_\mu^L|}\left[\int_{\Omega_\mu}\boldsymbol{\sigma}_\mu\cdot\delta\boldsymbol{\varepsilon}\,d\Omega_\mu\right], \tag{47}$$

$$\delta_\lambda\Pi_\mu(\boldsymbol{\varepsilon},\lambda,\tilde{\boldsymbol{u}}_\mu,\tilde{\lambda}_\mu)=\frac{|\boldsymbol{n}_m|}{|\Gamma_\mu^L|^2}\left[\int_{\Gamma_\mu^L}\delta\lambda\cdot[\![\boldsymbol{u}_\mu]\!]_{\mathbf{y}}\,d\Gamma_\mu^L\right], \tag{48}$$

$$\begin{aligned}\delta_{\tilde{\boldsymbol{u}}_\mu}\Pi_\mu(\boldsymbol{\varepsilon},\lambda,\tilde{\boldsymbol{u}}_\mu,\tilde{\lambda}_\mu)=\frac{1}{|\Gamma_\mu^L|}&\left[\int_{\Omega_\mu}\boldsymbol{\sigma}_\mu\cdot\nabla^s\delta\tilde{\boldsymbol{u}}_\mu\,d\Omega_\mu\right.\\&+\int_{\Gamma_\mu}\left[\tilde{\lambda}_\mu+\gamma\left([\![\boldsymbol{u}_\mu]\!]_{\mathbf{y}}-\boldsymbol{\delta}_\mu\right)\right]\cdot[\![\delta\tilde{\boldsymbol{u}}_\mu]\!]_{\mathbf{y}}\,d\Gamma_\mu+\\&\left.+\frac{|\boldsymbol{n}_m|}{|\Gamma_\mu^L|}\int_{\Gamma_\mu^L}\lambda\cdot[\![\delta\tilde{\boldsymbol{u}}_\mu]\!]_{\mathbf{y}}\,d\Gamma_\mu^L\right],\end{aligned} \tag{49}$$

$$\delta_{\tilde{\lambda}_\mu}\Pi_\mu(\boldsymbol{\varepsilon},\lambda,\tilde{\boldsymbol{u}}_\mu,\tilde{\lambda}_\mu)=\frac{1}{|\Gamma_\mu^L|}\left[\int_{\Gamma_\mu}\delta\tilde{\lambda}_\mu\cdot\left([\![\boldsymbol{u}_\mu]\!]_{\mathbf{y}}-\boldsymbol{\delta}_\mu\right)\,d\Gamma_\mu\right]. \tag{50}$$

The compatibility of scales is guaranteed equating the power variations at both scales

$$\delta\Pi(\boldsymbol{u},\lambda)=\delta\Pi_\mu(\boldsymbol{\varepsilon},\lambda,\boldsymbol{u}_\mu,\lambda_\mu)\,, \tag{51}$$

Taking into account (44) and (46) to (50),

$$\begin{aligned}&[\![\delta\boldsymbol{u}]\!]\cdot\lambda+[\![\boldsymbol{u}]\!]\cdot\delta\lambda\\&=\frac{1}{|\Gamma_\mu^L|}\left[\int_{\Omega_\mu}\boldsymbol{\sigma}_\mu\cdot\delta\boldsymbol{\varepsilon}\,d\Omega_\mu+\frac{|\boldsymbol{n}_m|}{|\Gamma_\mu^L|}\int_{\Gamma_\mu^L}\delta\lambda\cdot[\![\boldsymbol{u}_\mu]\!]_{\mathbf{y}}\,d\Gamma_\mu^L\right.\\&\quad+\int_{\Omega_\mu}\boldsymbol{\sigma}_\mu\cdot\nabla^s\delta\tilde{\boldsymbol{u}}_\mu\,d\Omega_\mu+\\&\quad+\int_{\Gamma_\mu}\left[\tilde{\lambda}_\mu+\gamma\left([\![\boldsymbol{u}_\mu]\!]_{\mathbf{y}}-\boldsymbol{\delta}_\mu\right)\right]\cdot[\![\delta\tilde{\boldsymbol{u}}_\mu]\!]_{\mathbf{y}}\,d\Gamma_\mu+\\&\quad\left.+\frac{|\boldsymbol{n}_m|}{|\Gamma_\mu^L|}\int_{\Gamma_\mu^L}\lambda\cdot[\![\delta\tilde{\boldsymbol{u}}_\mu]\!]_{\mathbf{y}}\,d\Gamma_\mu^L+\int_{\Gamma_\mu}\delta\tilde{\lambda}_\mu\cdot\left([\![\boldsymbol{u}_\mu]\!]_{\mathbf{y}}-\boldsymbol{\delta}_\mu\right)\,d\Gamma_\mu\right].\end{aligned} \tag{52}$$

The following consequences can be derived from Eq. (52).

3.2.3. Consequence 1. Micro-mechanical equilibrium problem. Unstable regime

Considering $\delta\boldsymbol{u}=0$ and $\delta\lambda=0$ in Eq. (52), the following equilibrium equations are obtained for the **RVE**

$$\begin{aligned}&\int_{\Omega_\mu}\boldsymbol{\sigma}_\mu\cdot\nabla^s\delta\tilde{\boldsymbol{u}}_\mu\,d\Omega_\mu+\int_{\Gamma_\mu}\left[\tilde{\lambda}_\mu+\gamma\left([\![\boldsymbol{u}_\mu]\!]_{\mathbf{y}}-\boldsymbol{\delta}_\mu\right)\right]\cdot[\![\delta\tilde{\boldsymbol{u}}_\mu]\!]_{\mathbf{y}}\,d\Gamma_\mu\\&\quad+\int_{\Gamma_\mu^L}\frac{|\boldsymbol{n}_m|}{|\Gamma_\mu^L|}\lambda\cdot[\![\delta\tilde{\boldsymbol{u}}_\mu]\!]_{\mathbf{y}}\,d\Gamma_\mu^L=0,\quad\forall\delta\tilde{\boldsymbol{u}}_\mu\in\tilde{\mathscr{V}}_\mu,\end{aligned} \tag{53}$$

$$\int_{\Gamma_\mu}\delta\tilde{\lambda}_\mu\cdot\left([\![\boldsymbol{u}_\mu]\!]_{\mathbf{y}}-\boldsymbol{\delta}_\mu\right)\,d\Gamma_\mu=0,\quad\forall\delta\tilde{\lambda}_\mu\in\tilde{\mathscr{W}}_\mu^{\Gamma_\mu^L}. \tag{54}$$

It is interesting to note that, these equilibrium equations are similar to those obtained for the stable regime (Eq. (27)) but the solution space $\tilde{\mathscr{W}}_\mu^{\Gamma_\mu^L}$ defined in Eq. (42) is more restricted than that of the stable regime $\mathscr{W}_\mu$ (Eq. (28)).

3.2.4. Consequence 2. Kinematical restriction and homogenization operator of the dual variable. Unstable regime

Considering $\delta\tilde{\boldsymbol{u}}_\mu=0$ and $\delta\tilde{\lambda}_\mu=0$ in Eq. (52), a kinematical consequence and the homogenization operator of the dual variable in the macro scale are obtained.

Kinematical restriction

Considering $\delta\lambda=0$, the following expression is obtained

$$[\![\delta\boldsymbol{u}]\!]\cdot\lambda=\frac{1}{|\Gamma_\mu^L|}\left[\int_{\Omega_\mu}\boldsymbol{\sigma}_\mu\cdot\nabla^s\delta\left(\boldsymbol{u}+\boldsymbol{\varepsilon}\cdot\left(\mathbf{y}-\mathbf{y}_0\right)+\tilde{\boldsymbol{u}}_\mu\right)\,d\Omega_\mu\right] \tag{55}$$

$$[\![\delta\boldsymbol{u}]\!]\cdot\lambda=\frac{1}{|\Gamma_\mu|}\left[\int_{\Omega_\mu}\boldsymbol{\sigma}_\mu\cdot\delta\boldsymbol{\varepsilon}\,d\Omega_\mu\right]. \tag{56}$$

The volumetric strain variation is due to the effect of the macro jump displacement over the **RVE**. Thus, from now, this component is denoted as $\delta\boldsymbol{\varepsilon}\to\delta\boldsymbol{\varepsilon}_{[\![\boldsymbol{u}]\!]}$. Introducing Axiom 1 en the last equation

$$\int_{\Gamma_\mu^L}\frac{|\Gamma_\mu^L|}{|\boldsymbol{n}_m|}\boldsymbol{\sigma}_\mu\cdot\left([\![\delta\boldsymbol{u}]\!]\otimes^s\boldsymbol{n}_\mu^L\right)\,d\Gamma_\mu^L=\left[\int_{\Omega_\mu}\boldsymbol{\sigma}_\mu\cdot\delta\boldsymbol{\varepsilon}_{[\![\boldsymbol{u}]\!]}\,d\Omega_\mu\right]. \tag{57}$$

Considering the integral property of the superficial Dirac delta,

$$\int_{\Gamma_\mu^L}(\bullet)\,d\Gamma_\mu^L=\int_{\Omega_\mu}\delta_\mu^{\Gamma_\mu^L}(\bullet)\,d\Omega_\mu,\quad with\quad\delta_\mu^{\Gamma_\mu^L}=\begin{cases}0 & \forall\mathbf{y}\in\Omega_\mu\setminus\Gamma_\mu^L\\ +\infty & \forall\mathbf{y}\in\Gamma_\mu\end{cases}, \tag{58}$$

where $\delta_\mu^{\Gamma_\mu^L}$ (with unit $[\text{length}]^{-1}$) is the Dirac distribution. Eq. (57) can be expressed as

$$\left[\int_{\Omega_\mu}\boldsymbol{\sigma}_\mu\cdot\delta_\mu^{\Gamma_\mu^L}\frac{|\Gamma_\mu^L|}{|\boldsymbol{n}_m|}\left([\![\delta\boldsymbol{u}]\!]\otimes^s\boldsymbol{n}_\mu^L\right)\,d\Omega_\mu\right]=\left[\int_{\Omega_\mu}\boldsymbol{\sigma}_\mu\cdot\delta\boldsymbol{\varepsilon}_{[\![\boldsymbol{u}]\!]}\,d\Omega_\mu\right]. \tag{59}$$

Finally, the kinematic consequence is obtained

$$\boldsymbol{\varepsilon}_{[\![\boldsymbol{u}]\!]}=\delta_\mu^{\Gamma_\mu^L}\frac{|\Gamma_\mu^L|}{|\boldsymbol{n}_m|}\left([\![\boldsymbol{u}]\!]\otimes^s\boldsymbol{n}_\mu^L\right). \tag{60}$$

- **Stable Regime**

(A1) Kinematical assumption in the scale transition

$$d\boldsymbol{\varepsilon}_\mu(\boldsymbol{y},t) = \nabla^s_{\boldsymbol{y}}\, d\boldsymbol{u}_\mu(\boldsymbol{y}) = d\boldsymbol{\varepsilon}(\boldsymbol{x},t) + \nabla^s_{\boldsymbol{y}}\, d\tilde{\boldsymbol{u}}_\mu(\boldsymbol{y}), \quad \forall \boldsymbol{y} \in \Omega_\mu$$

$$d\boldsymbol{\varepsilon}(\boldsymbol{x},t) = \frac{1}{|\Omega_\mu|}\int_{\Omega_\mu} d\boldsymbol{\varepsilon}_\mu(\boldsymbol{y},t)\, d\Omega_\mu + \frac{1}{|\Omega_\mu|}\int_{\Gamma_\mu} [\![d\boldsymbol{u}_\mu]\!]_{\boldsymbol{y}} \otimes^s \boldsymbol{n}_\mu\, d\Gamma_\mu$$

(A2) Principle of Multiscale virtual power

$$\boldsymbol{\sigma} \cdot \nabla^s_{\boldsymbol{x}}\, \delta\boldsymbol{u} = \frac{1}{|\Omega_\mu|}\left[\int_{\Omega_\mu} \boldsymbol{\sigma}_\mu \cdot \nabla^s_{\boldsymbol{y}}\, \delta\boldsymbol{u}_\mu\, d\Omega_\mu + \int_{\Gamma_\mu} \lambda_\mu \cdot [\![\delta\boldsymbol{u}_\mu]\!]_{\boldsymbol{y}}\, d\Gamma_\mu\right]$$

(C1) Micro mechanical equilibrium problem

$$\int_{\Omega_\mu} \boldsymbol{\sigma}_\mu \cdot \nabla^s_{\boldsymbol{y}}\, \delta\tilde{\boldsymbol{u}}_\mu\, d\Omega_\mu + \int_{\Gamma_\mu} \left(\lambda_\mu + \gamma\left([\![\tilde{\boldsymbol{u}}_\mu]\!]_{\boldsymbol{y}} - \boldsymbol{\delta}_\mu\right)\right) \cdot [\![\delta\tilde{\boldsymbol{u}}_\mu]\!]_{\boldsymbol{y}}\, d\Gamma_\mu = 0, \ \forall \delta\tilde{\boldsymbol{u}}_\mu \in \tilde{\mathscr{V}}_\mu,$$

$$\int_{\Gamma_\mu} \left([\![\tilde{\boldsymbol{u}}_\mu]\!]_{\boldsymbol{y}} - \boldsymbol{\delta}_\mu\right) \cdot\ \delta\lambda_\mu\, d\Gamma_\mu = 0, \qquad \forall \delta\tilde{\lambda}_\mu \in \tilde{\mathscr{W}}_\mu,$$

$$\tilde{\mathscr{V}}_\mu := \left\{ \boldsymbol{\varphi} \in \boldsymbol{H}^1(\Omega_\mu) \mid \int_{\Omega_\mu} \boldsymbol{\varphi}\, d\Omega_\mu = 0 \ \ and \ \ \int_{\partial\Omega_\mu} \boldsymbol{\varphi} \otimes^s \boldsymbol{\nu}\, d\partial\Omega_\mu \right\}$$

$$\tilde{\mathscr{W}}_\mu\left(\Omega_\mu \setminus \Gamma_\mu\right) = \left\{ \delta\lambda_\mu \mid \delta\lambda_\mu \in \mathbf{H}^{-\frac{1}{2}} \right\}.$$

(C2) Characterization of the macroscopic stress

$$\boldsymbol{\sigma}(\boldsymbol{x},t) = \frac{1}{|\Omega_\mu|}\int_{\Omega_\mu} \boldsymbol{\sigma}_\mu(\boldsymbol{y},t)\ d\Omega_\mu$$

Box I.

The structure of this consequence is similar to the axiom stated for the model in Ref. [31].

Homogenization operator of the dual variable

Now, considering $[\![\delta\boldsymbol{u}]\!] = 0$

$$[\![\boldsymbol{u}]\!] \cdot \delta\lambda = \frac{|\boldsymbol{n}_m|}{|\Gamma^L_\mu|^2}\int_{\Gamma^L_\mu} [\![\boldsymbol{u}_\mu]\!]_{\boldsymbol{y}} \cdot \delta\lambda\ d\Gamma^L_\mu, \tag{61}$$

where the homogenization operator of the dual variable is

$$[\![\boldsymbol{u}]\!] = \frac{|\boldsymbol{n}_m|}{|\Gamma^L_\mu|^2}\int_{\Gamma^L_\mu} [\![\boldsymbol{u}_\mu]\!]_{\boldsymbol{y}}\ d\Gamma^L_\mu. \tag{62}$$

The relevant equations of the proposed multi-scale model, are summarized in Boxes I and II.

3.3. Numerical implementation of the proposed model

The equilibrium equations (53) and (54) include an extra restriction in the space of kinematically admissible tractions in the localization $\tilde{\mathscr{W}}^{\Gamma^L_\mu}_\mu$ that couples with the space of kinematically admissible displacement fluctuations $\tilde{\mathscr{V}}_\mu$. Considering an interpolation operator $\mathbb{L}(\boldsymbol{s},t)$ for the Lagrangian field, the restriction over the perturbation can be expressed as

$$\left[\int_{\Gamma^L_\mu} \mathbb{L}(\boldsymbol{s},t)\ d\Gamma^L_\mu\right]\boldsymbol{x}^L = 0 \ \Rightarrow\ \boldsymbol{C}^L\boldsymbol{x}^L = \boldsymbol{0}, \tag{63}$$

where $\boldsymbol{x}^L$ are the nodal values of the Lagrangian field. Condition stated in Eq. (63) is analogous to the condition of the minimally restricted space for displacement fluctuation $\tilde{\mathscr{V}}_\mu$ [65]. There are two ways of fulfilling this restriction: considering null perturbation $\boldsymbol{x}^L = \boldsymbol{0}$ or imposing Eq. (63) (minimally restricted).

A schema of a localization in the **RVE** is shown in Fig. 6, where tractions $\tilde{\lambda}_\mu \in \Gamma^L_\mu$ (from now $\tilde{\lambda}^L_\mu$) is split in three groups: prescribed degrees of freedom $\tilde{\lambda}^{L^p}_\mu$, dependent degrees of freedom $\tilde{\lambda}^{L^d}_\mu$ and free degrees of freedom $\tilde{\lambda}^{L^f}_\mu$.

Supposing n^L Lagrange multipliers in the localization zone, in bi-dimensional (2D) problems the dimensions of matrix $\boldsymbol{C}^L$ is $2\times 2n^L$ and it can be grouped as follow

$$\begin{bmatrix}\boldsymbol{C}^{L^f} & \boldsymbol{C}^{L^d} & \boldsymbol{C}^{L^p}\end{bmatrix}\begin{bmatrix}\boldsymbol{x}^{L^f}\\ \boldsymbol{x}^{L^d}\\ \boldsymbol{x}^{L^p}\end{bmatrix} = \boldsymbol{0}, \tag{64}$$

where $\boldsymbol{x}^{L^p} = \boldsymbol{0}$ is prescribed, being a vector of order 2×1. The prescribed degrees of freedom should be chosen such that the matrix $\boldsymbol{C}^{L^d}$ of order 2×2 is invertible. Finally

$$\begin{bmatrix}\boldsymbol{C}^{L^f} & \boldsymbol{C}^{L^d}\end{bmatrix}\begin{bmatrix}\boldsymbol{x}^{L^f}\\ \boldsymbol{x}^{L^d}\end{bmatrix} = \boldsymbol{0} \ \Rightarrow\ \boldsymbol{x}^{L^d} = -\boldsymbol{C}^{L^{d^{-1}}}\boldsymbol{C}^{L^f}\boldsymbol{x}^{L^f} \ \Rightarrow\ \boldsymbol{x}^{L^d} = \boldsymbol{R}^L\boldsymbol{x}^{L^f}, \tag{65}$$

where $\boldsymbol{R}^L = -\boldsymbol{C}^{L^{d^{-1}}}\boldsymbol{C}^{L^f}$ is a matrix of order $2\times(2n^L-4)$ in 2D problems. After trivial algebraic manipulations, the system to be solved is

$$\mathbb{K}^L \cdot \begin{Bmatrix}\tilde{\boldsymbol{u}}\\ \tilde{\lambda}_\mu\\ \tilde{\lambda}^{L^f}_\mu\end{Bmatrix} - \begin{Bmatrix}\mathbb{R}_{\tilde{\boldsymbol{u}}}\\ \mathbb{R}_{\tilde{\lambda}_\mu}\\ \mathbb{R}_{\tilde{\lambda}^{L^f}_\mu} + \boldsymbol{R}^{L^T}\mathbb{R}_{\tilde{\lambda}^{L^d}_\mu}\end{Bmatrix} = \begin{Bmatrix}\boldsymbol{0}\\ \boldsymbol{0}\\ \boldsymbol{0}\end{Bmatrix}, \tag{66}$$

where $\tilde{\lambda}_\mu$ are the traction fluctuations in non localized cracks and the stiffness matrix $\mathbb{K}^L$ is given by the equation given in Box III.

- **Unstable Regime**

(A1) Equivalent kinematical assumption in the scale transition

$$d\lambda_\mu^L = \frac{|\boldsymbol{n}_m|}{|\Gamma_\mu^L|}\, d\lambda + d\tilde{\lambda}_\mu$$

$$d\lambda = \frac{1}{|\boldsymbol{n}_m|}\int_{\Gamma_\mu^L} d\lambda_\mu^L\, d\Gamma_\mu^L$$

(A2) Principle of Multiscale virtual power

$$[\![\delta\boldsymbol{u}]\!]\cdot\lambda + [\![\boldsymbol{u}]\!]\cdot\delta\lambda = \frac{1}{|\Gamma_\mu^L|}\left[\int_{\Omega_\mu}\boldsymbol{\sigma}_\mu\cdot\delta\boldsymbol{\varepsilon}\, d\Omega_\mu + \frac{|\boldsymbol{n}_m|}{|\Gamma_\mu^L|}\int_{\Gamma_\mu^L}\delta\lambda\cdot[\![\boldsymbol{u}_\mu]\!]_{\mathbf{y}}\, d\Gamma_\mu^L + \int_{\Omega_\mu}\boldsymbol{\sigma}_\mu\cdot\nabla^s\delta\tilde{\boldsymbol{u}}_\mu\, d\Omega_\mu + \right.$$
$$+\int_{\Gamma_\mu}\left[\tilde{\lambda}_\mu + \gamma\left([\![\boldsymbol{u}_\mu]\!]_{\mathbf{y}} - \boldsymbol{\delta}_\mu\right)\right]\cdot[\![\delta\tilde{\boldsymbol{u}}_\mu]\!]_{\mathbf{y}}\, d\Gamma_\mu +$$
$$\left.+\frac{|\boldsymbol{n}_m|}{|\Gamma_\mu^L|}\int_{\Gamma_\mu^L}\lambda\cdot[\![\delta\tilde{\boldsymbol{u}}_\mu]\!]_{\mathbf{y}}\, d\Gamma_\mu^L + \int_{\Gamma_\mu}\delta\tilde{\lambda}_\mu\cdot\left([\![\boldsymbol{u}_\mu]\!]_{\mathbf{y}} - \boldsymbol{\delta}_\mu\right)\, d\Gamma_\mu\right].$$

(C1) Micro mechanical equilibrium problem

$$\int_{\Omega_\mu}\boldsymbol{\sigma}_\mu\cdot\nabla^s\delta\tilde{\boldsymbol{u}}_\mu\, d\Omega_\mu + \int_{\Gamma_\mu}\left[\lambda_\mu + \gamma\left([\![\boldsymbol{u}_\mu]\!]_{\mathbf{y}} - \boldsymbol{\delta}_\mu\right)\right]\cdot[\![\delta\tilde{\boldsymbol{u}}_\mu]\!]_{\mathbf{y}}\, d\Gamma_\mu = 0, \quad \forall\delta\tilde{\boldsymbol{u}}_\mu\in\tilde{\mathscr{V}}_\mu,$$
$$\int_{\Gamma_\mu}\delta\tilde{\lambda}_\mu\cdot\left([\![\boldsymbol{u}_\mu]\!]_{\mathbf{y}} - \boldsymbol{\delta}_\mu\right)\, d\Gamma_\mu = 0, \qquad \forall\delta\tilde{\lambda}_\mu\in\tilde{\mathscr{W}}_\mu^{\Gamma_\mu^L}.$$

$$\tilde{\mathscr{V}}_\mu := \left\{\boldsymbol{\varphi}\in\boldsymbol{H}^1(\Omega_\mu)\mid \int_{\Omega_\mu}\boldsymbol{\varphi}\, d\Omega_\mu = 0 \;\; and \;\; \int_{\partial\Omega_\mu}\boldsymbol{\varphi}\otimes^s\boldsymbol{\nu}\, d\partial\Omega_\mu\right\}$$

$$\tilde{\mathscr{W}}_\mu^{\Gamma_\mu^L}\left(\Omega_\mu\setminus\Gamma_\mu\right) := \left\{\boldsymbol{\varphi}\in\mathbf{H}^{-\frac{1}{2}} \;\wedge\; \int_{\Gamma_\mu^L}\boldsymbol{\varphi}\, d\Gamma_\mu^L = 0\right\}.$$

(C2) Kinematical restriction and homogenization operator of the dual variable

$$\boldsymbol{\varepsilon}_{[\![\boldsymbol{u}]\!]} = \delta_\mu^{\Gamma_\mu^L}\frac{|\Gamma_\mu^L|}{|\boldsymbol{n}_m|}\left([\![\boldsymbol{u}]\!]\otimes^s\boldsymbol{n}_\mu^L\right).$$

$$[\![\boldsymbol{u}]\!] = \frac{|\boldsymbol{n}_m|}{|\Gamma_\mu^L|^2}\int_{\Gamma_\mu^L}[\![\boldsymbol{u}_\mu]\!]_{\mathbf{y}}\, d\Gamma_\mu^L.$$

Box II.

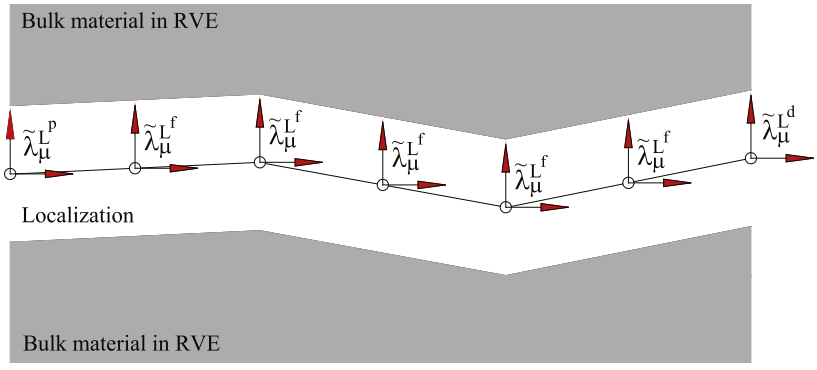

Fig. 6. A schema of the considered fields in the localization for the numerical implementation.

4. Numerical examples

4.1. Comparison with a analytical model

The multiscale model is first applied to the analysis of failure initiation in fibre reinforced composites under biaxial stress states. The **RVE** used for this purpose is presented in Fig. 7 and the constitutive properties of the materials are presented in Table 1. Failure initiation correspond to the onset of fibre/matrix debonding. The failure envelopes obtained for different boundary conditions, i.e. *linear (LBC), periodic (PBC)* and *uniform traction (TBC)*, are compared with the analytic

$$\mathbb{K}^L = \begin{bmatrix} \mathbb{K}_{\tilde{\boldsymbol{u}}\tilde{\boldsymbol{u}}} & \mathbb{K}_{\tilde{\boldsymbol{u}}\tilde{\lambda}_\mu} & \left(\mathbb{K}_{\tilde{\boldsymbol{u}}\tilde{\lambda}_\mu^{L^f}} + \mathbb{K}_{\tilde{\boldsymbol{u}}\tilde{\lambda}_\mu^{L^d}}\boldsymbol{R}^L\right) \\ \mathbb{K}_{\tilde{\lambda}_\mu\tilde{\boldsymbol{u}}} & \mathbb{K}_{\tilde{\lambda}_\mu\tilde{\lambda}_\mu} & \left(\mathbb{K}_{\tilde{\lambda}_\mu\tilde{\lambda}_\mu^{L^f}} + \mathbb{K}_{\tilde{\lambda}_\mu\tilde{\lambda}_\mu^{L^d}}\boldsymbol{R}^L\right) \\ \left(\mathbb{K}_{\tilde{\lambda}_\mu^{L^f}\tilde{\boldsymbol{u}}} + \boldsymbol{R}^{L^T}\mathbb{K}_{\tilde{\lambda}_\mu^{L^d}\tilde{\boldsymbol{u}}}\right) & \left(\mathbb{K}_{\tilde{\lambda}_\mu^{L^f}\tilde{\lambda}_\mu} + \boldsymbol{R}^{L^T}\mathbb{K}_{\tilde{\lambda}_\mu^{L^d}\tilde{\lambda}_\mu}\right) & \left(\mathbb{K}_{\tilde{\lambda}_\mu^{L^f}\tilde{\lambda}_\mu^{L^f}} + \mathbb{K}_{\tilde{\lambda}_\mu^{L^f}\tilde{\lambda}_\mu^{L^d}}\boldsymbol{R}^L + \boldsymbol{R}^{L^T}\mathbb{K}_{\tilde{\lambda}_\mu^{L^d}\tilde{\lambda}_\mu^{L^f}} + \boldsymbol{R}^{L^T}\mathbb{K}_{\tilde{\lambda}_\mu^{L^d}\tilde{\lambda}_\mu^{L^d}}\boldsymbol{R}^L\right) \end{bmatrix}.$$

Box III.

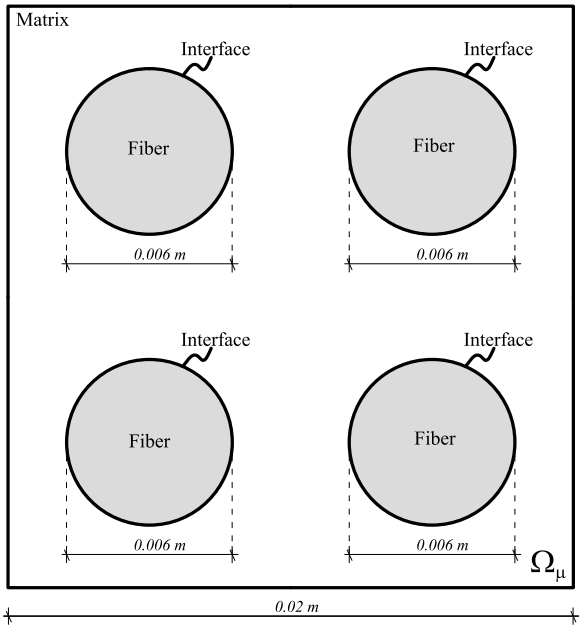

Fig. 7. **RVE** for the fibre reinforced composite.

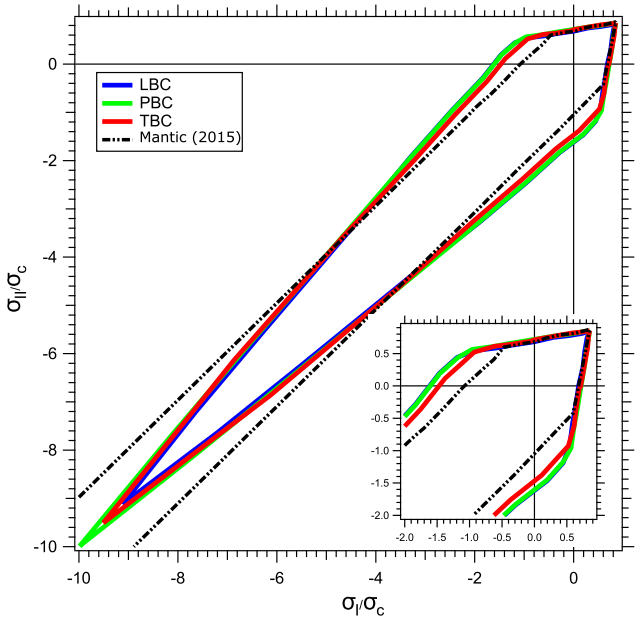

Fig. 8. Obtained results for different **RVE** boundary conditions.

Table 1
Material properties for the **RVE** of Fig. 8.

	Matrix	Fibre	Interface
Young modulus E [MPa]	68890	413040	–
Poisson modulus	0.33	0.20	–
Critical stress σ_c [MPa]	–	-	30
Fracture energy G_c [N/mm]	–	-	0.1

Table 2
Material properties for **RVE**s with cracks crossing the border $\partial\Omega_\mu$.

	Material 1	Material 2	Interface
Young modulus E [MPa]	3900	86900	–
Poisson modulus	0.37	0.23	–
Critical stress σ_c [MPa]	–	-	30
Fracture energy G_c [N/mm]	–	-	1

solution obtained by Mantič et al. [66] in Fig. 8 where stress are related to the interface strength σ_c. A good agreement with the analytical solution [66] is obtained for the tension–tension regime. The analytical model proposed in [66] presents some limitations in the compression zone that can be overcome with the present approach that is able to capture failure under equibiaxial compression.

4.2. Objectivity of the response

Although the complete multiscale approach was presented in the previous sections, in order to have a simple interpretation of the results, a single macro material point is considered in all examples. For the numerical tests it is assumed that, before the ellipticity loss, the macroscopic point is subjected to a macroscopic strain history of $\varepsilon_{22}(x,t)$. After the ellipticity loss, in the macroscopic point a traction history $\lambda(x,t)$ is injected. The prescribed values of macro strain and traction are given by

$$\varepsilon_{22}(x,t) = \alpha(t) \quad \forall t \le t_L \quad \text{and} \quad \lambda(x,t) = -\beta(t)\,\boldsymbol{\sigma}\cdot\boldsymbol{n} \quad \forall t > t_L\,, \tag{67}$$

where $\alpha(t)$ and $\beta(t)$ are prescribed functions, see Fig. 9.

The presented approach is general and allows changing the solution spaces when instability is detected at the macro-scale. But, without lost of generality, the kinematically admissible spaces used for the **RVE** are the minimally restricted for $\tilde{\mathscr{V}}_\mu$, and the trivial space $\tilde{\mathscr{W}}_\mu^{L_\mu}$ with null perturbations for the localized domain.

Two simple geometries, the first with plane fracture and the second with a tortuous fracture presented in Fig. 10(a) and (d) respectively, are analysed. Fig. 10(b–c) and (e–f) are periodical repetitions of the core **RVE**, introduced to shows the objectivity of the model [67]. The material properties used for this example are detailed in Table 2.

The problem is solved using both the classical (Section 3.1) and the proposed (Section 3.2) multi-scale approaches. The macro scale stress–strain responses obtained are plotted in Fig. 11, 12 and 13 respectively. If classical formulation is used, injecting the macroscopic strain in the micro-scale to obtain the stress at the macro scale, that is $\boldsymbol{\varepsilon} \longmapsto$ **RV E** $\longmapsto \boldsymbol{\sigma}$, a non-objective response is observed in Fig. 11 after the ellipticity loss, both in the case of plane fracture (Fig. 11(a)) and tortuous fracture (Fig. 11(b)). Fig. 11(c) presents a polar plot of the acoustic tensor determinant and it shows that, in both cases, the normal vector of the macroscopic crack is $\boldsymbol{n} = [0\ 1]$.

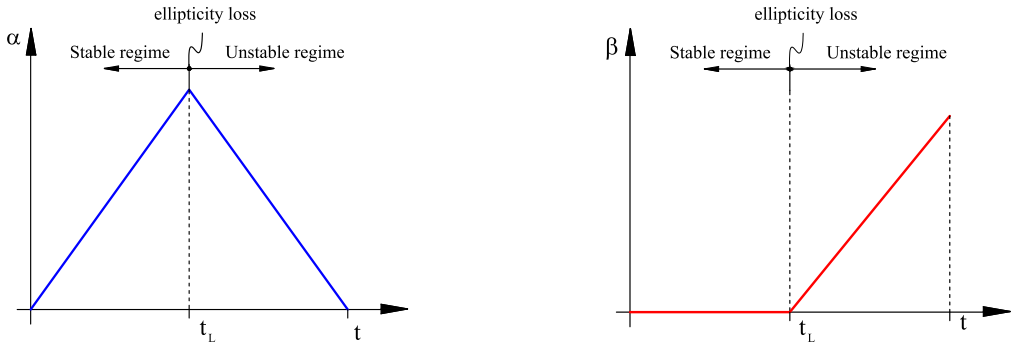

(a) $\alpha(t)$. (b) $\beta(t)$.

Fig. 9. Prescribed history of macroscopic functions.

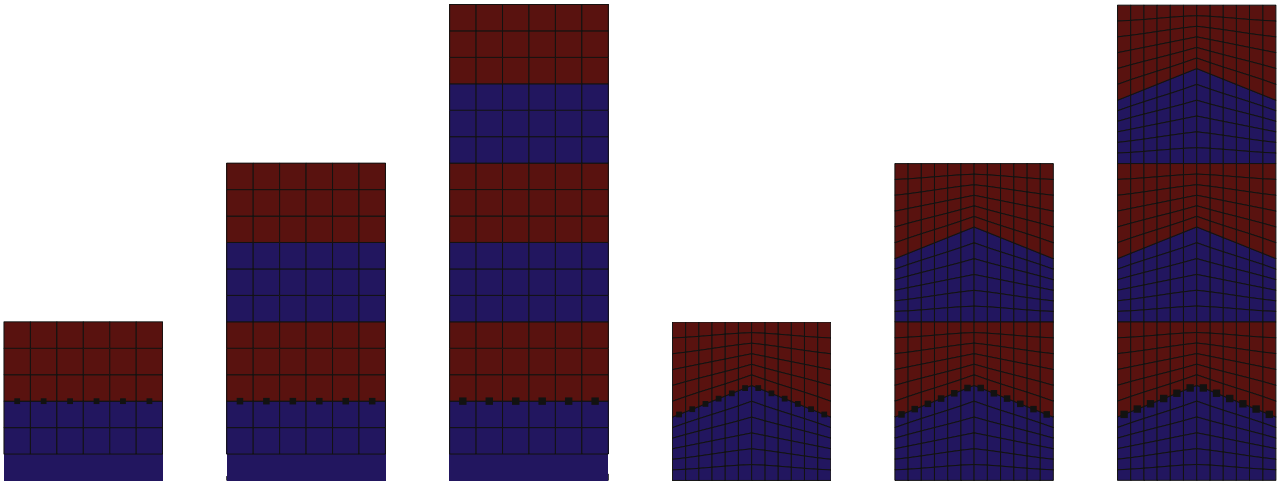

(a) **RVE**N°1. (b) **RVE**N°2. (c) **RVE**N°3. (d) **RVE**N°1. (e) **RVE**N°2. (f) **RVE**N°3.

Fig. 10. Localized zone detection in the **RVE**. Plane and tortuous fracture.

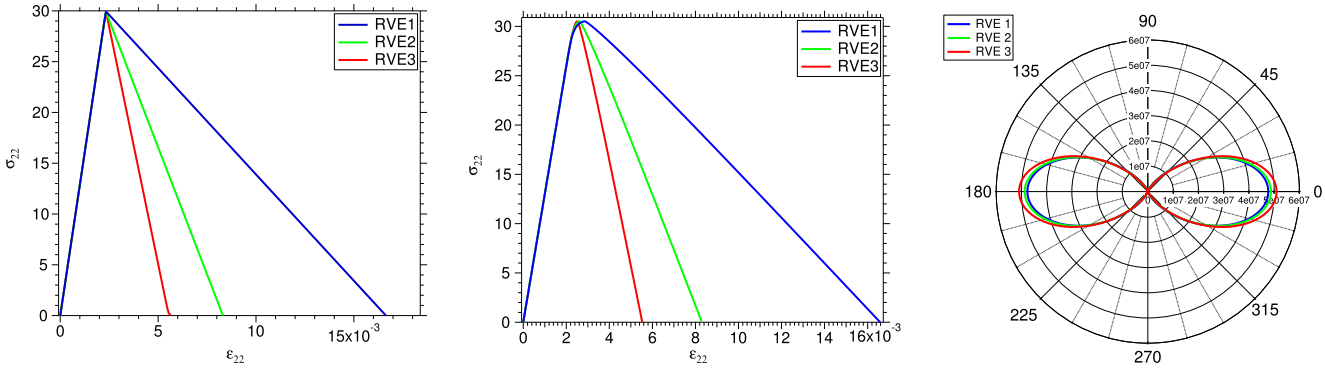

(a) Stress–strain response for **RVE**s presented in Fig. 10 (plane fracture).

(b) Stress–strain response for **RVE**s presented in Fig. 10 (tortuous fracture).

(c) Loss of ellipticity for **RVE**s presented in Fig. 10.

Fig. 11. Stress–strain response using the classical formulation.

When the proposed model is activated in time $t = t_N$ after the localization, the macroscopic crack traction is injected in the localized domain (elements with black square points in Fig. 10), recovering the homogenized separation for the macro scale that is $\lambda = -\boldsymbol{\sigma} \cdot \boldsymbol{n} \longmapsto$ **RV E** $\longmapsto [\![\boldsymbol{u}]\!]$. The results using this strategy are showed in Fig. 12 for **RVE**s with plain localization and in Fig. 13 for tortuous localization.

It can be observed in Figs. 12 and 13, that the curves for all the proposed cells are coincident, concluding in a objective macroscopic traction-separation response independently of the micro-cell. The regularization length for the scale transition in these examples, are $|\boldsymbol{n}_m| = 10$ and $|\Gamma_\mu^L| = 10$ for the **RVE**s in Fig. 10(a–c), and $|\boldsymbol{n}_m| = 10$ and $|\Gamma_\mu^L| = 10.7703$ for **RVE**s in Fig. 10(d–f). The relation between those

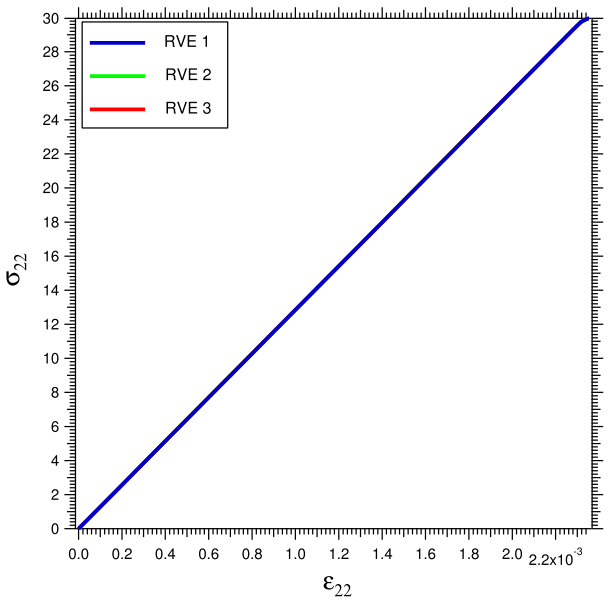

(a) Stress–strain homogenized response.

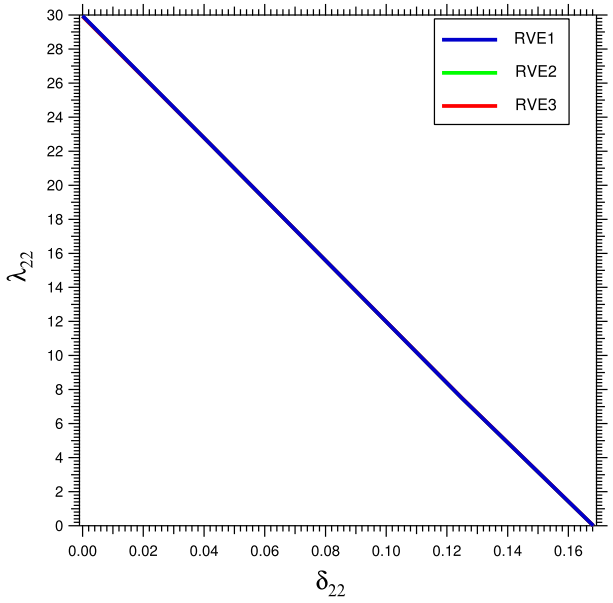

(b) Traction-separation homogenized response.

Fig. 12. Results obtained with the proposed model for **RVE**s with plane fracture (Fig. 10(a–c)).

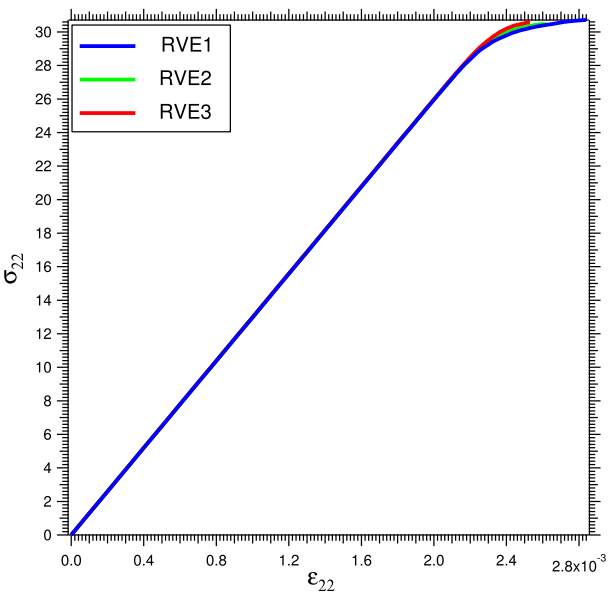

(a) Stress–strain homogenized response.

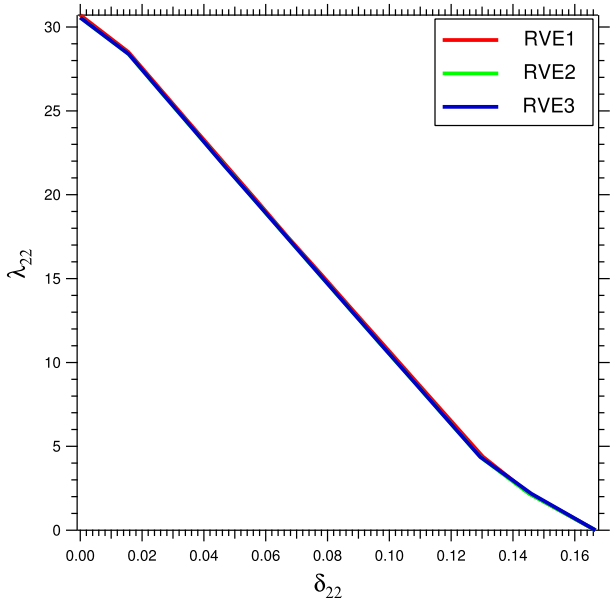

(b) Traction-separation homogenized response.

Fig. 13. Results obtained with the proposed model for **RVE**s with tortuous fracture (10(d–f)).

quantities is known as the tortuosity index $\theta = \frac{|\Gamma_\mu|}{|\boldsymbol{n}_m|}$ [31]. It goes from 1 for plain fractures to ∞ for the ideal scenario of an infinitely tortuous crack path. For the proposed examples, the tortuosity index are $\theta = 1$ (Fig. 10(a–c)) and $\theta = 1.07703$ (Fig. 10(d–f)).

Observation 4.1. *Stress–strain curves presented in Fig. 13(a) are not coincident during the hardening phase. This is due a shape effect introduced by the proposed **RVE**s. Curves become totally coincident when the same aspect ratio is considered. **RVE** N°4 and N°5 presented in Fig. 14(a–b) are considered now, obtaining coincident responses.*

4.3. RVEs with regular and rigid inclusions

Three **RVE**s with regular geometry, consisting in a matrix reinforced with rigid inclusions crossed by tortuous interfaces, are presented in Fig. 15. **RVE** N°1 is a square cell of 10 [mm] in each side and the other **RVE**s are generated as a periodic repetition of this cell. The mechanical parameters used for these example are presented in Table 3. Analogously to the case of quasi-brittle composite (concrete, reinforced epoxy, etc.), the Material 1-Material 1 interface has different properties compared with interface Material 1-Material 2 interface. The numerical

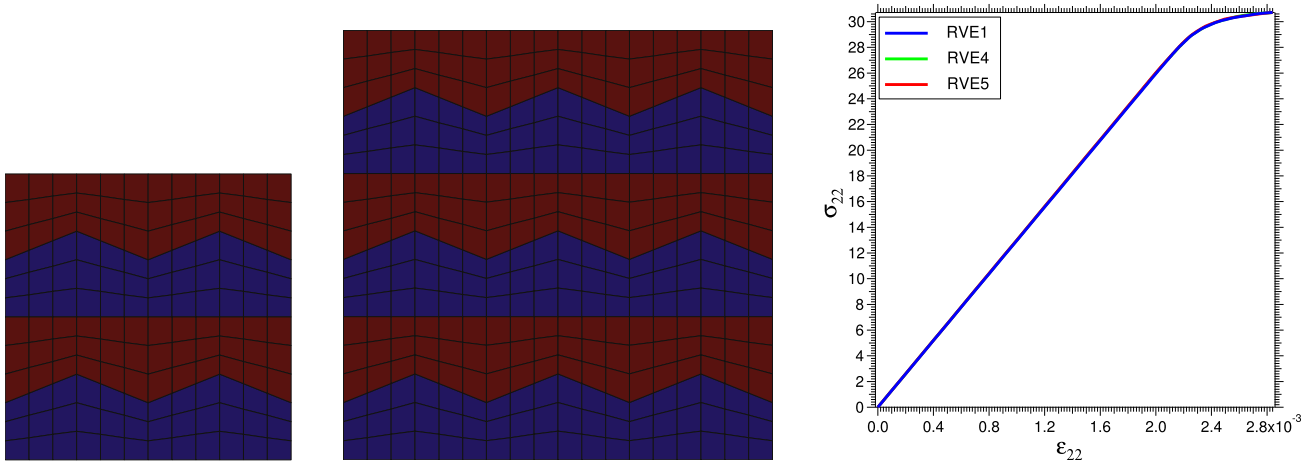

(a) **RVE** N°4. (b) **RVE** N°5. (c) Stress–strain response in stable regime.

Fig. 14. **RVE** without shape effect in stable regime. Classical model.

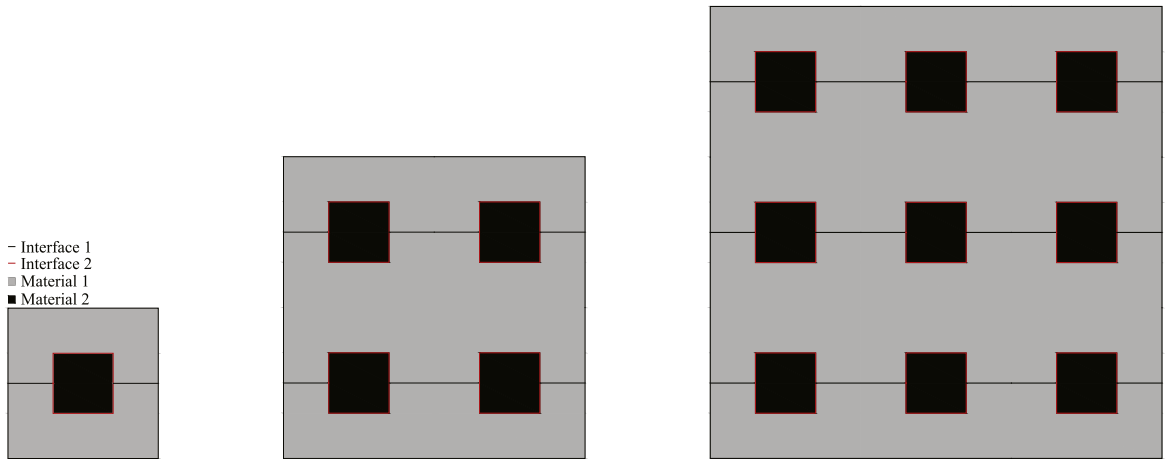

(a) **RVE** N°1. (b) **RVE** N°2. (c) **RVE** N°3.

Fig. 15. **RVE**s containing rigid inclusions with regular geometry.

Table 3
Material properties for **RVE**s with regular rigid inclusions.

	Material 1	Material 2	Mat. 1-Mat. 2 interface
Young Mod. E[MPa]	3900	86900	–
Poisson Mod.	0.37	0.23	–
Critical tension σ_c [MPa]	70	–	35
Fracture energy G_c [N/mm]	0.5	–	0.5

simulations are carried out under the same macroscopic conditions as presented in Section 4.2.

The homogenized results are presented in Fig. 16. The stress–strain curves until the localization time t_L are presented in Fig. 16(a). It can be seen that, the curve obtained for **RVE** N°1, is similar to those obtained with the other **RVEs**, but it extends to a final strain of $\varepsilon_{22} = 4.5 \times 10^{-2}$ higher than the macro-localization onset of $\varepsilon_{22} = 3.2 \times 10^{-2}$ obtained for the other **RVE**s. For all cases, the peak stress is coincident ($\sigma_{22_{peak}} =$ 68 [MPa]).

The normal vector of the localization in the macro scale is $\boldsymbol{n} =$ [0 1] for all cases. Although they are damage and dissipate energy, vertical interfaces of material 1-material 2 are not considered as part of Γ_μ^L, because they do not fulfil condition (36). Hence, the macroscopic traction is not injected on those vertical interfaces. In this sense, it can be concluded that a damaged element in the **RVE** is a necessary but not sufficient condition to be part of the localized micro domain where the traction obtained from the macro should be injected. For these cases, the regularization length parameters for scale transition in localization are $|\Gamma_\mu^L| = 14$ [μm], $|\Gamma_\mu^L| = 56$ [μm] and $|\Gamma_\mu^L| = 120$ [μm] for **RVE** N°1, N°2 y N°3 respectively, and with tortuosity index $\theta = 1$ for all cases.

Fig. 16(b) shows the results using the proposed model. The three curves are coincident, being the increase of the localized zone, proportional to the **RVE** size increasement. In this sense, it can be concluded that the **RVE**N°2 is representative of the used micro structure, for the used micro-scale boundaries. The behaviour is bi-linear due the combination of interface properties.

4.4. Multi-scale modelling of a transverse fracture

A transverse fracture example of a composite reinforced with longitudinal fibres is proposed in this case. Five **RVE**s with the same volumetric fraction $V_f = 30\%$ are showed in Fig. 17. **RVE** N°1 in Fig. 17(a) contains 14 fibres and 60 μm of side, **RVE** N°2 in Fig. 17(b) contains 18 fibres and 68 μm of side, **RVE** N°3 in Fig. 17(c) contains 20 fibres of 72 μm of side, **RVE** N°4 in Fig. 17(d) contains 25 fibres and 80.9 μm of side, and **RVE** N°5 in Fig. 17(e) contains 30 fibres and 88.6 μm of side. The distribution of the inclusions is aleatory and it was obtained with the Monte Carlo method. The material properties are presented in Table 4. To avoid the **RVE** shape effect previously discussed, square cells are considered.

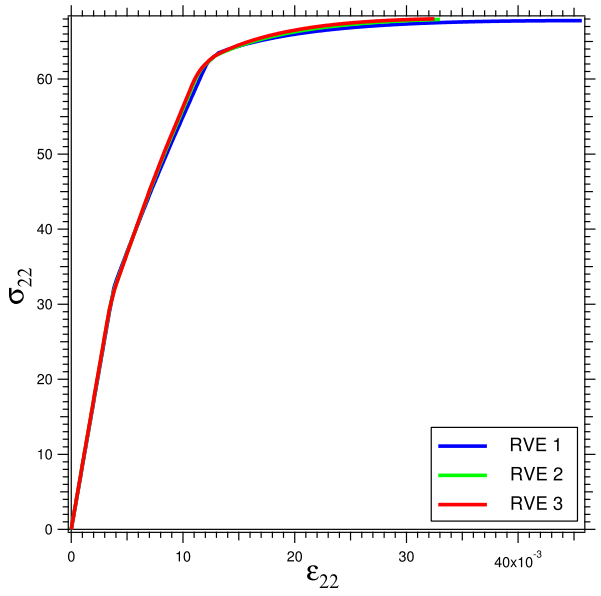

(a) Stress–strain (before localization).

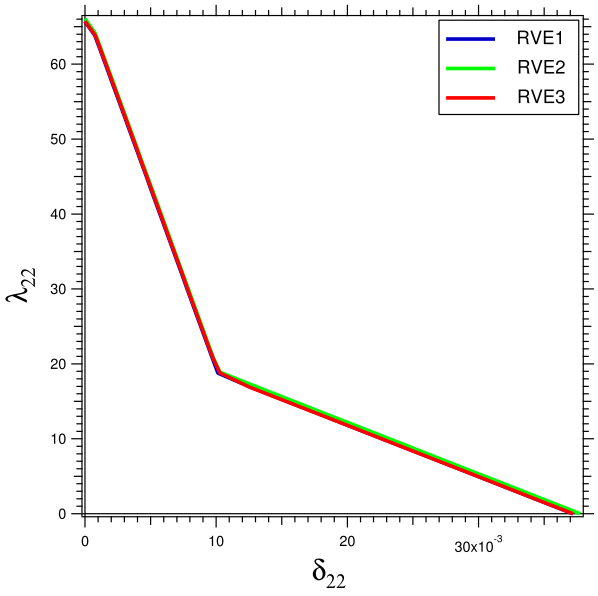

(b) Traction-separation (after localization).

Fig. 16. Results obtained for **RVE**s presented in Fig. 15.

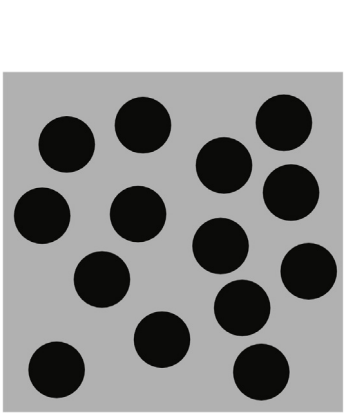

(a) **RVE** N°1.

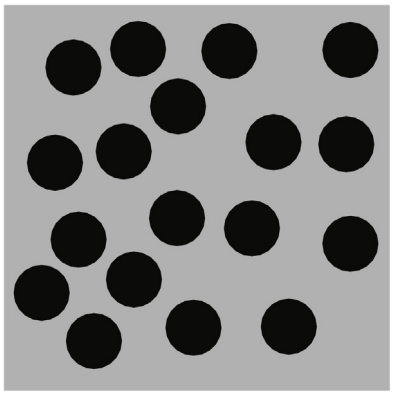

(b) **RVE** N°2.

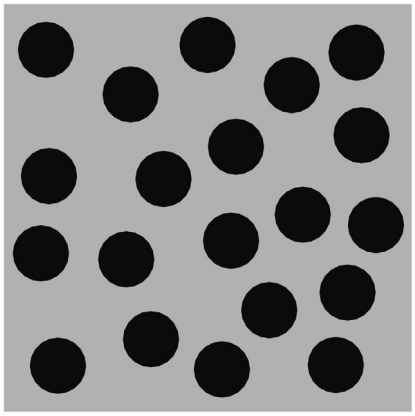

(c) **RVE** N°3.

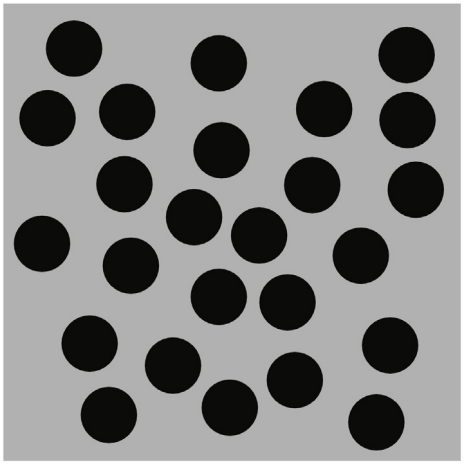

(d) **RVE** N°4.

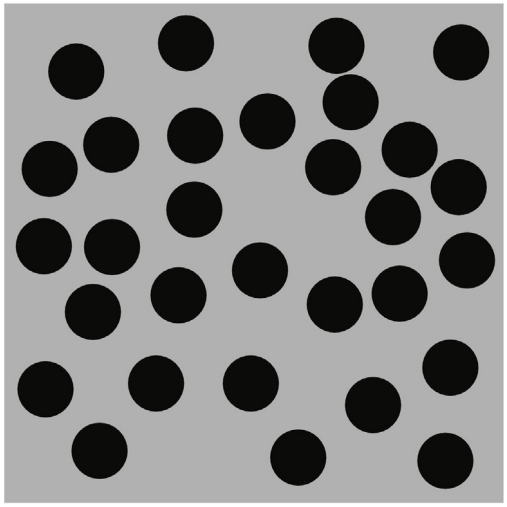

(e) **RVE** N°5.

Fig. 17. Adopted **RVE**s for transverse multi-scale fracture. Fibre volume fraction $V_f = 30\%$.

Table 4
Material properties of the epoxy matrix reinforced with longitudinal fibres.

	Matrix	Fibre	Matrix–fibre
Young modulus E [MPa]	3900	86900	–
Poisson modulus	0.37	0.23	–
Critical tension σ_c [MPa]	50	–	25
Fracture energy G_c [N/mm]	0.5	–	0.5

Table 5
Parameters for the proposed models for each **RVE**.

	$\boldsymbol{n}_x$	$\boldsymbol{n}_y$	θ	$\boldsymbol{\varepsilon}_{t_L}$	$\boldsymbol{\sigma}_p$ [MPa]
RVE N° 1	0.010355	0.99995	1.2455	0.0123	36.372
RVE N° 2	−0.1217	0.99257	1.2797	0.0113	34.942
RVE N° 3	−0.042804	0.99908	1.2082	0.0125	36.987
RVE N° 4	−0.056638	0.99839	1.3278	0.0092	37.124
RVE N° 5	0.010318	0.99995	1.2429	0.0098	36.307

The initial constitutive tensor for **RVE**s N°1 , N°2, N°3, N°4 and N°5 are presented in (68). It can be seen that the composite material is not orthotropic due the aleatoric distribution of the inclusions, coupling shear with the normal stresses (not null constants $\mathbb{C}_{1133}$ and $\mathbb{C}_{2233}$).

$$
\begin{aligned}
\mathbb{C}^e_{\mathbf{RVE}N°1} &= \begin{bmatrix} 10364.73 & 5695.26 & 13.23 \\ 5695.26 & 10514.45 & -23.48 \\ 13.23 & -23.47 & 2334.22 \end{bmatrix}, \\
\mathbb{C}^e_{\mathbf{RVE}N°2} &= \begin{bmatrix} 10413.63 & 5665.23 & 3.22 \\ 5665.23 & 10288.87 & 29.86 \\ 3.22 & 29.86 & 2327.32 \end{bmatrix}, \\
\mathbb{C}^e_{\mathbf{RVE}N°3} &= \begin{bmatrix} 10364.88 & 5645.93 & 18.47 \\ 5645.93 & 10350.33 & 8.98 \\ 18.47 & 8.98 & 2328.92 \end{bmatrix}, \\
\mathbb{C}^e_{\mathbf{RVE}N°4} &= \begin{bmatrix} 10341.07 & 5612.17 & -5.64 \\ 5612.17 & 10495.15 & 14.66 \\ -5.64 & 14.66 & 2323.43 \end{bmatrix}, \\
\mathbb{C}^e_{\mathbf{RVE}N°5} &= \begin{bmatrix} 10405.09 & 5624.79 & 9.75 \\ 5624.79 & 10416.98 & -53.42 \\ 9.75 & -53.42 & 2342.32 \end{bmatrix}.
\end{aligned}
\tag{68}
$$

The determinant of the acoustic tensor is plotted in a polar graph in Fig. 18, at the localization time t_L, corresponding to a strain $\boldsymbol{\varepsilon}_{t_L}$. The localization damage configuration of the proposed **RVE**s, is presented in Fig. 19. It can be observed that, for all cases, due to the fibre arrangement, the localization is concentrated towards one side of the cell. The localization parameters obtained from the acoustic tensor analysis that are used to initiate the unstable phase analysis with the proposed model are presented in Table 5, where $\boldsymbol{n}_x$ and $\boldsymbol{n}_y$ are the components of the normal vector $\boldsymbol{n}$, and $\boldsymbol{\sigma}_p$ is the peak stress.

It can be observed that the macro crack normal has a strong dependence on the inclusions distribution within the **RVE**, being out of phase with respect to the applied load direction. The tortuosity factor θ is greater than 1 ($1.2082 < \theta < 1.3278$) for all cases due the tortuous nature of the localization. The obtained peak stresses have a limited variation of approximately 5%, although a different scenario is reached for the localization strain where the maximum difference is about a 26%.

The results of the proposed model are presented in Figs. 19 and 20. Fig. 19 shows the deformation patterns of the different **RVE**s corresponding to the localization time t_L. The stress–strain response calculated with the classical model in stable regime, is showed in Fig. 20(a), the plotted stress correspond to $\boldsymbol{\sigma}_{nn} = \boldsymbol{\sigma}\cdot(\boldsymbol{n}\otimes\boldsymbol{n})$. It is observed that the curves corresponding to the different **RVE**s are coincident until

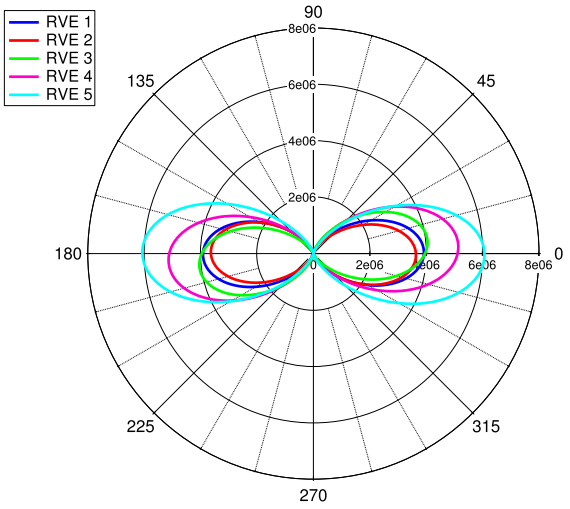

Fig. 18. Ellipticity loss for **RVE**s presented in Fig. 17.

strain $\varepsilon_{22} = 0.006$, diverging after that until the lost of ellipticity. The homogenized traction-separation curves for the macro scale obtained with the proposed model, are presented in Fig. 20(b). All curves are almost coincident with little variation, except for the case of **RVE** N°1. It can be observed that the **RVE** N°2 has a displacement value of 4.10×10^{-3} when the traction reach a null value. This feature is not observed in the others **RVE**s, where the traction tends to zero asymptotically. The limit displacement of **RVE** N°2 can be attributed to the fact that both sides of the **RVE** remains connected by one element that does not localize.

Unlike the previous examples where the micro-structural configuration is regular in this case it is not possible to conclude the existence of an **RVE** for the proposed boundary conditions. The only way to get a certain conclusion is comparing the results obtained with the multi-scale setting with a direct numerical simulation (DNS).

5. Conclusions

A variationally consistent multi-scale model to homogenize the traction-separation law once the constitutive tensor $\mathbb{C}$ loses its ellipticity, has been formulated and discussed in this paper. The model is developed using the axiomatic philosophy presented by Blanco and Giusti [26]. During the stable phase of the material, a classical multi-scale scheme is used. When a crack is propagated in the macro-structure, the traction in the discontinuity surface $\mathcal{S}$ is introduced as a boundary condition over a localization domain Γ^L_μ of the **RVE**, reformulating the concept of injection operator proposed in Ref [47]. After solving the equilibrium equations, the jump of the discontinuity in the macro-scale is calculated. It has been shown that the equilibrium equations in the stable and unstable regime, differs in a simple additional restriction in the space of admissible Lagrange multipliers field $\mathscr{W}_\mu$ migrating to a space of admissible Lagrange field fluctuations $\tilde{\mathscr{W}}_\mu^{\Gamma^L_\mu}$. The kinematical consequence of the proposed injection is also proved, showing the same mathematical structure than the proposed by others researchers Ref. [31]. A discussion about the numerical implementation of the space $\tilde{\mathscr{W}}_\mu^{\Gamma^L_\mu}$ is also presented in Section 3.3, showing a form analogous to that of the classical space $\mathscr{V}_\mu$ [65].

Some numerical examples to study the softening regime at macroscopic scale are presented. All these examples are based on the **RVE** concept. The proposed multi-scale model showed a good performance being the calculated macro-scale traction-separation law, both for plane and tortuous crack paths, is objective with respect to the **RVE** size [67]. Some **RVE**s consisting on a soft matrix with rigid inclusions were also presented, showing the ability of the proposed formulation to deal with

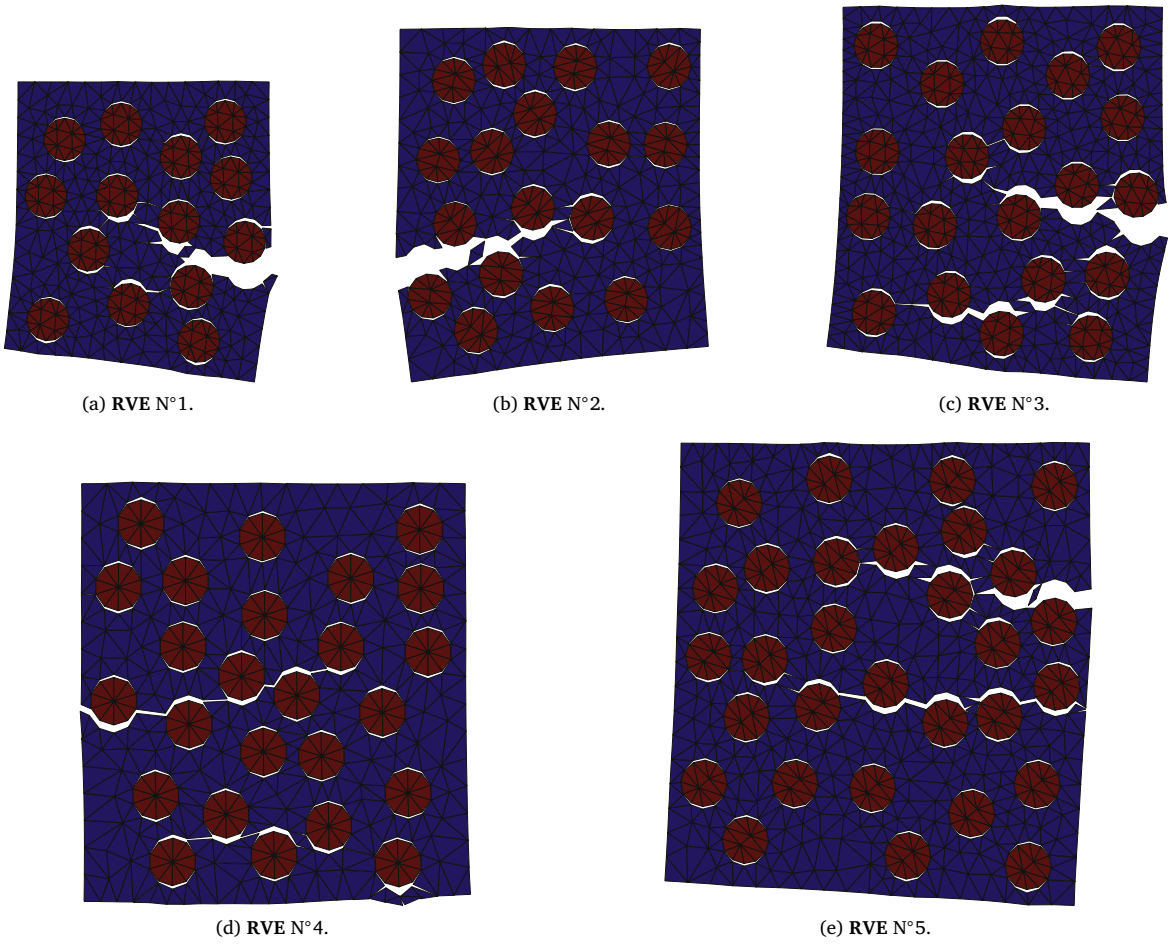

(a) **RVE** N°1. (b) **RVE** N°2. (c) **RVE** N°3.

(d) **RVE** N°4. (e) **RVE** N°5.

Fig. 19. Localization for **RVE**s presented in Fig. 17. Fibre volumetric fraction $V_f = 30\%$.

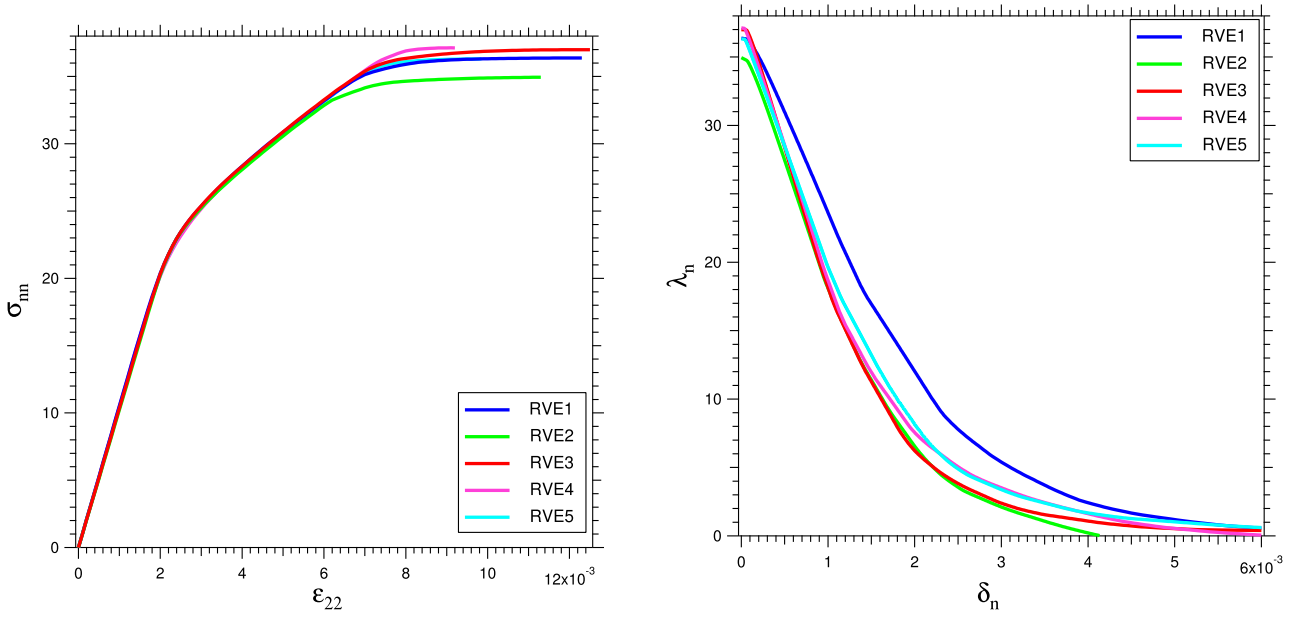

(a) Stress–strain curves (before localization). (b) Traction-separation curves (after localization).

Fig. 20. Computed results for **RVE**s presented in Fig. 17.

this context where, due the material anisotropy, the load direction and the direction of the discontinuity normal $\boldsymbol{n}$, are not coincident.

In the stable regime *linear*, *periodic* or *traction* boundary conditions can be used for the **RVE**. For the unstable regime the examples were solved by combining the minimally restricted space for the displacement fluctuation field in the **RVE** boundary $\partial\boldsymbol{\Omega}_{\mu}$, and the trivial space for the Lagrange multipliers fluctuation field in the localization Γ_{μ}^{L}. This election is not mandatory and the used of other combinations of spaces will be analysed in future papers.

Acknowledgements

The authors wish to thank the financial support of National Agency for Scientific and Technological Promotion (PICT 2013 1740), National Scientific and Technological Research Council (CONICET) and National University of Tucumán research Council (PIUNT 26E/520). The work of S.M. Giusti was partially supported by the European Research Council under the European Union's Seventh Framework Programme (FP/2007–2013)/ERC Grant Agreement n. 320815 (ERC Advanced Grant Project "Advanced tools for computational design of engineering materials" COMP-DES-MAT).

References

[1] Andrei V. Metrikine, Harm Askes, One-dimensional dynamically consistent gradient elasticity models derived from a discrete microstructure: Part 1: Generic formulation, Eur. J. Mech. A Solids 21 (2002) 555–572.
[2] Andrei V. Metrikine, Harm Askes, One-dimensional dynamically consistent gradient elasticity models derived from a discrete microstructure: Part 2: Static and dynamic response, Eur. J. Mech. A Solids 21 (2002) 573–588.
[3] José Miranda Guedes, Noboru Kikuchi, Preprocessing, postprocessing for materials based on the homogenization method with adaptive finite element methods, Comput. Methods Appl. Mech. Engrg. 83 (1990) 143–198.
[4] R.H.J. Peerlings, N.A. Fleck, Computational evaluation of strain gradient elasticity constants, Int. J. Multiscale Comput. Eng. 2 (2004) 1543–1649.
[5] J.C. López-Realpozo, R. Rodríguez-Ramos, R. Guiovart-Díaz, J. Bravo-Castillero, J.A. Otero, F.J. Sabina, F. Lebon, S. Dumont, I. Sevostianov, Effective elastic shear stiffness of a periodic fibrous composite with non-uniform imperfect contact between the matrix and the fibers, Int. J. Solids Struct. 51 (2014) 1253–1262.
[6] F. Lebon, S. Dumont, R. Rizzoni, J.C. López-Realpozo, R. Guiovart-Díaz, R. Rodríguez-Ramos, J. Bravo-Castillero, F.J. Sabina, Soft and hard anisotropic interface in composite materials, Composites Part B 90 (2016) 58–68.
[7] J.A. Otero, R. Rodríguez-Ramos, G. Monsivais, Computation of effective properties in elastic composites with different inclusion shapes and under imperfect contact, J. Math. Model. Appl. Sci. 40 (9) (2016) 3290–3310.
[8] R. Guiovart-Díaz, R. Rodríguez-Ramos, J.C. López-Realpozo, J. Bravo-Castillero, J.A. Otero, F.J. Sabina, F. Lebon, S. Dumont, Analysis of fibrous elastic composites with nonuniform imperfect adhesion, Acta Mech. 227 (1) (2016) 57–73.
[9] D. Guinovart-Sanjuán, R. Rodríguez-Ramosa, R. Guinovart-Díaza, J. Bravo-Castilleroa, F.J. Sabinab, J. Merodioc, F. Lebond, S. Dumontd, A. Concif, Effective properties of regular elastic laminated shell composite, Composites B 87 (2016) 12–20.
[10] H.S. Park, W.K. Liu, An introduction and tutorial on multiple-scale analysis in solids, Comput. Methods Appl. Mech. Engrg. 193 (2004) 1733–1772.
[11] J.T. Oden, S. Prudhomme, A. Romkes, P.T. Bauman, Multi scale modelling of physical phenomena: Adaptative control models, SIAM J. Sci. Comput. 28 (2006) 2359–2389.
[12] H.J. Bohm, A Short introduction to basic aspects of continuum micromechanics, ILSB Report, 2016.
[13] J.D. Eshelby, The determination of the elastic field of an ellipsoidal inclusion, and related problems, Proc. R. Soc. 241 (1957) 376–396.
[14] T. Mori, K. Tanaka, Average stress in the matrix and average elastic energy of materials with misfitting inclusions, Acta Metall. 21 (1973) 571–574.
[15] L. Brassart, H.M. Inglis, L. Delannay, I. Doghri, P.H. Geubelle, An extended Mori–Tanaka homogenization scheme for finite strain modeling of debonding in particle-reinforced elastomers, Comput. Mater. Sci. 45 (2009) 611–616.
[16] Z. Hashin, S. Shtrikman, A variational approach to the theory of the elastic behaviour of multiphase materials, J. Mech. Phys. Solids 11 (1963) 127–140.
[17] Z. Hashin, Analysis of composite materials. A survey, J. Appl. Mech. 50 (1983) 481–505.
[18] J. Willis, Variational and related methods for the overall properties of composites, Adv. Appl. Mech. 21 (1981) 1–78.
[19] V. Belsky, M.W. Beall, J. Fish, M.S. Shephard, S. Gomaa, Computer-aided multiscale modeling tools for composite materials and structures, Int. J. Comput. Syst. Engng. 6 (1995) 213–223.
[20] S. Ghosh, K.H. Lee, S. Moorthy, Two scale analysis of heterogeneous elastic–plastic materials with asymptotic homogenization and Voronoi cell finite element model, Comput. Meth. Appl. Mech. Engng. 132 (1996) 63–116.
[21] K.H. Lee, S. Ghosh, Small deformation multi-scale analysis of heterogeneous materials with the Voronoi cell finite element model and homogenization theory, Comput. Mater. Sci. 7 (1996) 131–146.
[22] N. Moes, M. Cloirec, P. Cartraud, J.F. Remacle, A computational approach to handle complex microstructure geometries, Comput. Methods Appl. Mech. Engrg. 192 (2003) 3163–3177.
[23] T.I. Zohdi, J.T. Oden, G.J. Rodin, Hierarchical modeling of heterogeneous bodies, Comput. Methods Appl. Mech. Engrg. 138 (1996) 273–289.
[24] V.P. Nguyen, M. Stroeven, L.J. Sluysn, Multiscale continuous and discontinuous modeling of heterogeneous materials: A review on recent developments, J. Multiscal. Model. 3 (2011) 229–270.
[25] A. Gurson, Continuum theory of ductile rupture by void nucleation and growth - Part I: Yield criteria and flow rules for porous ductile media, J. Engng. Mater. Technol. ASME 99 (1977) 2–15.
[26] P.J. Blanco, S.M. Giusti, Thermomechanical multiscale constitutive modeling: Accounting for microstructural thermal effects, J. Elasticity 111 (2013).
[27] F. Feyel, J.L. Chaboche, FE^2 multiscale approach for modelling the elastoviscoplastic behaviour of long fibre sic/ti composite materials, Comput. Meth. App. Mech. Eng. 183 (2000) 309–330.
[28] K. Matous, M. Kulkarni, P. Geubelle, Multiscale cohesive failure modeling of heterogeneous adhesives, J. Mech. Phys. Solids 56 (2008) 1511–1533.
[29] T. Belytschko, S. Loehnert, J.H. Song, Multiscale aggregating discontinuities: A method for circumventing loss of material stability, Internat. J. Numer. Methods Engrg. 73 (2008) 869–894.
[30] P.J. Blanco, P.J. Sanchez, E.A. de Souza Neto, R.A. Feijóo, Variational foundations and generalized unified theory of rve-based multiscale models, Arch. Comput. Methods Eng. 23 (2016) 191–253.
[31] S. Toro, P.J. Sánchez, P.J. Blanco, E.A. de Souza Neto, A.E. Huespe, R.A. Feijóo, Multiscale formulation for material failure accounting for cohesive cracks at the macro and micro scales, Int. J. Plast. 76 (2016) 75–110.
[32] P. Moseley, J. Oswald, T. Belytschko, Adaptive atomistic-to-continuum modeling of propagating defects, Internat. J. Numer. Methods Engrg. 92 (2012) 835–856.
[33] Jinghong Fan, Ross J. Stewart, Xiangguo Zeng, A multiscale method for dislocation nucleation and seamlessly passing scale boundaries, Int. J. Plast. 27 (2011) 2103–2124.
[34] O. Lloberas-Valls, Multiscale domain decomposition analysis of quasi-brittle materials (Ph.D. thesis), Faculty of Civil Engineering and Geosciences at Delft University of Technology, 2013.
[35] A. Caggiano, G. Etse, Coupled thermo–mechanical interface model for concrete failure analysis under high temperature, Comput. Methods Appl. Mech. Engrg. 289 (2015) 498–516.
[36] A.A. Rahimabadi, Error Controlled Adaptive Multiscale Method for Fracture in Polycrystalline Materials (Ph.D. thesis), Cardiff University, 2014.
[37] C.V. Verhoosel, J.C. Remmers, M.A. Gutierrez, R. de Borst, Computational homogenization for adhesive and cohesive failure in quasi-static solids, Int. J. Numer. Methods Eng. 83 (2010) 1155–1179.
[38] V.P. Nguyen, O. Lloberas-Valls, M. Stroeven, L.J. Sluys, Homogenization-based multiscale crack modelling: from micro-diffusive damage to macrocraks, Comput. Methods Appl. Mech. Engrg. 200 (2011) 1220–1236.
[39] V.P. Nguyen, O. Lloberas-Valls, M. Stroeven, L.J. Sluys, Computational homogenization for multiscale crack modeling. Implementation and computational aspects, Int. J. Numer. Methods Eng. 89 (2012) 192–226.
[40] T.J. Massart, R.H.J. Peerlings, M.G.D. Geers, An enhanced multi-scale approach for masonry wall computations with localization of damage, Int. J. Numer. Methods Eng. 5 (2007) 1022–1059.
[41] V.G. Kouznetsova, M.G.D. Geers, W.A.M. Brekelmans, Multi-scale constitutive modeling of heterogeneous materials with a gradient-enhanced computational homogenization scheme, Int. J. Numer. Methods Eng. 54 (2002) 1235–1260.
[42] M.G.D. Geers, V.G. Kouznetsova, W.A.M. Brekelmans, Multi-scale computational homogenization: Trends and challenges, J. Comput. Appl. Math. 234 (2010) 2175–2182.
[43] M.G.D. Geers, V.G. Kouznetsova, W.A.M. Brekelmans, Gradient-enhanced computational homogenization for the micro-macro scale transition, J. Phys. IV 5 (2001) 45–52.
[44] V.G. Kouznetsova, M.G.D. Geers, W.A.M. Brekelmans, Multi-scale second-order computational homogenization of multi-phase materials: a nested finite element solution strategy, Comput. Methods Appl. Mech. Eng. 51 (2004) 5525–5550.
[45] E. Souza Neto, R. Feijoo, Variational foundations of multiscale constitutive models of solids, LNCC internal report, 2008.
[46] S. Toro, Modelado de falla de materiales mediante formulaciones multiescala (Ph.D. thesis), Universidad Nacional del Litoral, 2014.
[47] P.J. Sánchez, P.J. Blanco, A.E. Huespe, R.A. Feijóo, Failure-oriented multi-scale variational formulation: Micro-structures with nucleation and evolution of softening bands, Comput. Methods Appl. Mech. Engrg. 257 (2013) 221–247.
[48] J. Oliver, M. Caicedo, E. Roubin, A.E. Huespe, Continuum approach to computational multi-scale modelling of fracture, Key Eng. Mater. 627 (2015) 349–352.

[49] N.A. Labanda, S.M. Giusti, B.M. Luccioni, Meso-scale fracture simulation using an augmented Lagrangian approach, Int. J. Damage Mech. (2016). http://dx.doi.org/10.1177/1056789516671092.
[50] F. Cazes, M. Coret, A. Combescure, A two-field modified Lagrangian formulation for robust simulations of extrinsic cohesive zone models, Comput. Mech. 51 (6) (2013) 865–884.
[51] S. Toro, P.J. Sánchez, J.M. Podestá, P.J. Blanco, A.E. Huespe, A.R. Feijóo, Cohesive surface model for fracture based on a two-scale formulation: computational implementation aspects, Comput. Mech. 58 (2016) 549–585.
[52] E.W.C. Coenen, V.G. Kouznetsova, M.G.D. Geers, Novel boundary conditions for strain localization analyses in microstructural volume elements, Int. J. Numer. Methods Eng. 90 (2012) 1–21.
[53] E.W.C. Coenen, V.G. Kouznetsova, M.G.D. Geers, Multi-scale continuous–discontinuous framework for computational-homogenization–localization, J. Mech. Phys. Solids 60 (2012) 1486–1507.
[54] E. Lorentz, A mixed interface finite element for cohesive zone models, Comput. Meth. Appl. Mech. Engng. 198 (2008) 302–317.
[55] M. Fortin, R. Glowinski, Augmented lagrangian methods: application to the numerical solution of boundary-value problems, in: North-Holland - Studies in Mathematics and its Applications, 1983.
[56] F. Brezzi, On the existence, uniqueness and approximation of saddle point problems arising from Lagrangian multipliers, RAIRO Anal. Numer. 8 (1974) 129–151.
[57] J. Baiges, R. Codina, F. Henke, A symmetric method for weakly imposing Dirichlet boundary conditions in embedded finite element meshes, Internat. J. Numer. Methods Engrg. 90 (2012) 636–658.
[58] E. Bechet, N. Moes, B. Wohlmuth, A stable Lagrange multiplier space for stiff interface conditions within the extended finite element method, Internat. J. Numer. Methods Engrg. 78 (8) (2009) 931–954.
[59] C. Talon, A. Curnier, A model of adhesion coupled to contact and friction, Eur. J. Mech. A Solids 22 (2003) 545–565.
[60] J. Rice, The localization of plastic deformation, in: Theoretical and Applied Mechanics, 14th IUTAM Congress, 1976, pp. 207–220.
[61] J. Rice, J. Rudnicki, A note on some features of the theory of localization of deformation, Int. J. Solids Struct. 16 (1980) 597–605.
[62] J. Mandel, Plasticité Classique et viscoplasticité, in: CISM Lecture Notes, 1971.
[63] R. Hill, A self consistent mechanics of composites materials, J. Mech. Phys. Solids 12 (1965) 213–222.
[64] J.R. Rice, J.W. Rudnicki, A note on some features of the theory of localization of deformation, Int. J. Solids Struct. 16 (1980) 7–605.
[65] S.M. Giusti, P.J. Blanco, E.A. de Souza Neto, R.A. Feijóo, An assessment of the Gurson yield criterion by a computational multi-scale approach, Eng. Comput. 26 (2009) 281–301.
[66] V. Mantič, L. Távara, A. Blázquez, E. Graciani, F. París, A linear elastic-brittle interface model: application for the onset and propagation of a fibre-matrix interface crack under biaxial transverse loads, Int. J. Fract. 195 (1–2) (2015) 15–38.
[67] I.M. Gitman, H. Askes, L.J. Sluys, Representative volume: Existence and size determination, Eng. Fract. Mech. 74 (2007) 2518–2534.